

DESY-02-142
September 2002

Leading proton production in e^+p collisions at HERA

ZEUS Collaboration

Abstract

Events with a final-state proton carrying a large fraction of the proton beam momentum, $x_L > 0.6$, and the square of the transverse momentum $p_T^2 < 0.5$ GeV 2 , have been studied in e^+p collisions with the ZEUS detector at HERA. Data with different photon virtualities were used: $Q^2 < 0.02$ GeV 2 , $0.1 < Q^2 < 0.74$ GeV 2 and $3 < Q^2 < 254$ GeV 2 , corresponding to integrated luminosities of 0.9, 1.85 and 3.38 pb $^{-1}$. The cross sections are given as a function of x_L , p_T^2 , Q^2 and the Bjorken scaling variable, x . The ratio of the cross section for leading proton production to the inclusive e^+p cross section shows only a mild dependence on Q^2 and on x . In the region $0.6 < x_L < 0.97$, the relative yield of protons is only a weak function of x_L .

The ZEUS Collaboration

S. Chekanov, D. Krakauer, J.H. Loizides¹, S. Magill, B. Musgrave, J. Repond, R. Yoshida
Argonne National Laboratory, Argonne, Illinois 60439-4815 ⁿ

M.C.K. Mattingly

Andrews University, Berrien Springs, Michigan 49104-0380

P. Antonioli, G. Anzivino², G. Bari, M. Basile, L. Bellagamba, D. Boscherini, A. Bruni, G. Bruni, G. Cara Romeo, M. Chiarini, L. Cifarelli, F. Cindolo, A. Contin, M. Corradi, S. De Pasquale, P. Giusti, G. Iacobucci, G. Levi, A. Margotti, T. Massam, R. Nania, C. Nemoz³, F. Palmonari, A. Pesci, G. Sartorelli, Y. Zamora Garcia⁴, A. Zichichi
University and INFN Bologna, Bologna, Italy ^e

G. Aghuzumtsyan, D. Bartsch, I. Brock, J. Crittenden⁵, S. Goers, H. Hartmann, E. Hilger, P. Irrgang, H.-P. Jakob, A. Kappes, U.F. Katz⁶, O. Kind, E. Paul, J. Rautenberg⁷, R. Renner, H. Schnurbusch, A. Stifutkin, J. Tandler, K.C. Voss, M. Wang, A. Weber
Physikalisches Institut der Universität Bonn, Bonn, Germany ^b

D.S. Bailey⁸, N.H. Brook⁸, J.E. Cole, B. Foster, G.P. Heath, H.F. Heath, T. Namsoo, S. Robins, E. Rodrigues⁹, M. Wing

H.H. Wills Physics Laboratory, University of Bristol, Bristol, United Kingdom ^m

R. Ayad¹⁰, M. Capua, L. Iannotti¹¹, A. Mastroberardino, M. Schioppa, G. Susinno
Calabria University, Physics Department and INFN, Cosenza, Italy ^e

J.Y. Kim, Y.K. Kim, J.H. Lee, I.T. Lim, M.Y. Pac¹²

Chonnam National University, Kwangju, Korea ^g

A. Caldwell¹³, M. Helbich, X. Liu, B. Mellado, Y. Ning, S. Paganis, Z. Ren, W.B. Schmidke, F. Sciulli

Nevis Laboratories, Columbia University, Irvington on Hudson, New York 10027 ^o

J. Chwastowski, A. Eskreys, J. Figiel, K. Olkiewicz, P. Stopa, L. Zawiejski
Institute of Nuclear Physics, Cracow, Poland ⁱ

L. Adamczyk, T. Bołd, I. Grabowska-Bołd, D. Kisielewska, A.M. Kowal, M. Kowal, T. Kowalski, M. Przybycień, L. Suszycki, D. Szuba, J. Szuba¹⁴

Faculty of Physics and Nuclear Techniques, University of Mining and Metallurgy, Cracow, Poland ^p

A. Kotański¹⁵, W. Słomiński¹⁶

Department of Physics, Jagellonian University, Cracow, Poland

L.A.T. Bauerick¹⁷, U. Behrens, I. Bloch, K. Borras, V. Chiochia, D. Dannheim, M. Derrick¹⁸,
G. Drews, J. Fourletova, A. Fox-Murphy¹⁹, U. Fricke, A. Geiser, F. Goebel¹³, P. Göttlicher²⁰,
O. Gutsche, T. Haas, W. Hain, G.F. Hartner, S. Hillert, U. Kötz, H. Kowalski²¹, G. Kram-
berger, H. Labes, D. Lelas, B. Löhr, R. Mankel, I.-A. Melzer-Pellmann, M. Moritz²²,
D. Notz, M.C. Petrucci²³, A. Polini, A. Raval, U. Schneekloth, F. Selonke²⁴, H. Wes-
soleck, R. Wichmann²⁵, G. Wolf, C. Youngman, W. Zeuner

Deutsches Elektronen-Synchrotron DESY, Hamburg, Germany

A. Lopez-Duran Viani²⁶, A. Meyer, S. Schlenstedt

DESY Zeuthen, Zeuthen, Germany

G. Barbagli, E. Gallo, C. Genta, P. G. Pelfer

University and INFN, Florence, Italy^e

A. Bamberger, A. Benen, N. Coppola, H. Raach

Fakultät für Physik der Universität Freiburg i.Br., Freiburg i.Br., Germany^b

M. Bell, P.J. Bussey, A.T. Doyle, C. Glasman, J. Hamilton, S. Hanlon, A. Lupi²⁷,
D.H. Saxon, I.O. Skillicorn

Department of Physics and Astronomy, University of Glasgow, Glasgow, United Kingdom^m

I. Gialas

Department of Engineering in Management and Finance, Univ. of Aegean, Greece

B. Bodmann, T. Carli, U. Holm, K. Klimek, N. Krumnack, E. Lohrmann, M. Milite,
H. Salehi, S. Stonjek²⁸, K. Wick, A. Ziegler, Ar. Ziegler

Hamburg University, Institute of Exp. Physics, Hamburg, Germany^b

C. Collins-Tooth, C. Foudas, R. Gonçalo⁹, K.R. Long, F. Metlica, D.B. Miller, A.D. Tap-
per, R. Walker

Imperial College London, High Energy Nuclear Physics Group, London, United Kingdom^m

P. Cloth, D. Filges

Forschungszentrum Jülich, Institut für Kernphysik, Jülich, Germany

M. Kuze, K. Nagano, K. Tokushuku²⁹, S. Yamada, Y. Yamazaki

Institute of Particle and Nuclear Studies, KEK, Tsukuba, Japan^f

A.N. Barakbaev, E.G. Boos, N.S. Pokrovskiy, B.O. Zhautykov

*Institute of Physics and Technology of Ministry of Education and Science of Kazakhstan,
Almaty,
Kazakhstan*

H. Lim, D. Son

Kyungpook National University, Taegu, Korea^g

F. Barreiro, O. González, L. Labarga, J. del Peso, I. Redondo³⁰, J. Terrón, M. Vázquez
Departamento de Física Teórica, Universidad Autónoma Madrid, Madrid, Spain^l

M. Barbi, A. Bertolin, F. Corriveau, S. Gliga, S. Lainesse, S. Padhi, D.G. Stairs
Department of Physics, McGill University, Montréal, Québec, Canada H3A 2T8^a

T. Tsurugai
Meiji Gakuin University, Faculty of General Education, Yokohama, Japan

A. Antonov, P. Danilov, B.A. Dolgoshein, D. Gladkov, V. Sosnovtsev, S. Suchkov
Moscow Engineering Physics Institute, Moscow, Russia^j

R.K. Dementiev, P.F. Ermolov, Yu.A. Golubkov, I.I. Katkov, L.A. Khein, I.A. Korzhavina, V.A. Kuzmin, B.B. Levchenko, O.Yu. Lukina, A.S. Proskuryakov, L.M. Shcheglova, N.N. Vlasov, S.A. Zotkin
Moscow State University, Institute of Nuclear Physics, Moscow, Russia^k

C. Bokel, J. Engelen, S. Grijpink, E. Koffeman, P. Kooijman, E. Maddox, A. Pellegrino, S. Schagen, E. Tassi, H. Tiecke, N. Tuning, J.J. Velthuis, L. Wiggers, E. de Wolf
NIKHEF and University of Amsterdam, Amsterdam, Netherlands^h

N. Brümmer, B. Bylsma, L.S. Durkin, J. Gilmore, C.M. Ginsburg, C.L. Kim, T.Y. Ling
*Physics Department, Ohio State University, Columbus, Ohio 43210*ⁿ

S. Boogert, A.M. Cooper-Sarkar, R.C.E. Devenish, J. Ferrando, G. Grzelak, S. Patel, M. Rigby, M.R. Sutton, R. Walczak
Department of Physics, University of Oxford, Oxford United Kingdom^m

R. Brugnera, R. Carlin, F. Dal Corso, S. Dusini, A. Garfagnini, S. Limentani, A. Longhin, A. Parenti, M. Posocco, L. Stanco, M. Turcato
Dipartimento di Fisica dell' Università and INFN, Padova, Italy^e

E.A. Heaphy, B.Y. Oh, P.R.B. Saull³¹, J.J. Whitmore³²
Department of Physics, Pennsylvania State University, University Park, Pennsylvania 16802^o

Y. Iga
Polytechnic University, Sagamihara, Japan^f

G. D'Agostini, G. Marini, A. Nigro
Dipartimento di Fisica, Università 'La Sapienza' and INFN, Rome, Italy^e

C. Cormack³³, J.C. Hart
Rutherford Appleton Laboratory, Chilton, Didcot, Oxon, United Kingdom^m

E. Barberis³⁴, C. Heusch, W. Lockman, J.T. Rahn, H.F.-W. Sadrozinski, A. Seiden,
D.C. Williams

University of California, Santa Cruz, California 95064 ⁿ

I.H. Park

Department of Physics, Ewha Womans University, Seoul, Korea

N. Pavel

Fachbereich Physik der Universität-Gesamthochschule Siegen, Germany

H. Abramowicz, A. Gabareen, S. Kananov, A. Kreisel, A. Levy

Raymond and Beverly Sackler Faculty of Exact Sciences, School of Physics, Tel-Aviv University, Tel-Aviv, Israel ^d

T. Abe, T. Fusayasu, S. Kagawa, T. Kohno, T. Tawara, T. Yamashita

Department of Physics, University of Tokyo, Tokyo, Japan ^f

R. Hamatsu, T. Hirose²⁴, M. Inuzuka, H. Kaji, S. Kitamura³⁵, K. Matsuzawa, T. Nishimura
S. Patel

Tokyo Metropolitan University, Department of Physics, Tokyo, Japan ^f

M. Arneodo³⁶, N. Cartiglia, R. Cirio, M. Costa, M.I. Ferrero, L. Lamberti³⁷, S. Maselli,
V. Monaco, C. Peroni, M. Ruspa, R. Sacchi, A. Solano, A. Staiano

Università di Torino, Dipartimento di Fisica Sperimentale and INFN, Torino, Italy ^e

R. Galea, T. Koop, G.M. Levman, J.F. Martin, A. Mirea, A. Sabetfakhri

Department of Physics, University of Toronto, Toronto, Ontario, Canada M5S 1A7 ^a

J.M. Butterworth, C. Gwenlan, R. Hall-Wilton, T.W. Jones, M.S. Lightwood

Physics and Astronomy Department, University College London, London, United Kingdom ^m

J. Ciborowski³⁸, R. Ciesielski³⁹, R.J. Nowak, J.M. Pawlak, B. Smalska⁴⁰, J. Sztuk⁴¹,
T. Tymieniecka⁴², A. Ukleja⁴², J. Ukleja, A.F. Żarnecki

Warsaw University, Institute of Experimental Physics, Warsaw, Poland ^q

M. Adamus, P. Plucinski

Institute for Nuclear Studies, Warsaw, Poland ^q

Y. Eisenberg, L.K. Gladilin⁴³, D. Hochman, U. Karshon

Department of Particle Physics, Weizmann Institute, Rehovot, Israel ^c

D. Kçira, S. Lammers, L. Li, D.D. Reeder, A.A. Savin, W.H. Smith

Department of Physics, University of Wisconsin, Madison, Wisconsin 53706 ⁿ

A. Deshpande, S. Dhawan, V.W. Hughes, P.B. Straub

Department of Physics, Yale University, New Haven, Connecticut 06520-8121 ⁿ

S. Bhadra, C.D. Catterall, S. Fourletov, S. Menary, M. Soares, J. Standage
Department of Physics, York University, Ontario, Canada M3J 1P3 ^a

¹ also affiliated with University College London, UK

² now at Università di Perugia, Dipartimento di Fisica, Perugia, Italy

³ now at E.S.R.F., Grenoble, France

⁴ now at Inter American Development Bank, Washington DC, USA

⁵ now at Cornell University, Ithaca, NY, USA

⁶ on leave of absence at University of Erlangen-Nürnberg, Germany

⁷ supported by the GIF, contract I-523-13.7/97

⁸ PPARC Advanced fellow

⁹ supported by the Portuguese Foundation for Science and Technology (FCT)

¹⁰ now at Temple University, Philadelphia, PA, USA

¹¹ now at Consoft Sistemi, Torino, Italy

¹² now at Dongshin University, Naju, Korea

¹³ now at Max-Planck-Institut für Physik, München, Germany

¹⁴ partly supported by the Israel Science Foundation and the Israel Ministry of Science

¹⁵ supported by the Polish State Committee for Scientific Research, grant no. 2 P03B 09322

¹⁶ member of Dept. of Computer Science

¹⁷ now at Fermilab, Batavia, IL, USA

¹⁸ on leave from Argonne National Laboratory, USA

¹⁹ now at R.E. Austin Ltd., Colchester, UK

²⁰ now at DESY group FEB

²¹ on leave of absence at Columbia Univ., Nevis Labs., NY, USA

²² now at CERN

²³ now at INFN Perugia, Perugia, Italy

²⁴ retired

²⁵ now at Mobilcom AG, Rendsburg-Büdelsdorf, Germany

²⁶ now at Deutsche Börse Systems AG, Frankfurt/Main, Germany

²⁷ now at University of Pisa, Italy

²⁸ now at Univ. of Oxford, Oxford, UK

²⁹ also at University of Tokyo

³⁰ now at LPNHE Ecole Polytechnique, Paris, France

³¹ now at National Research Council, Ottawa, Canada

³² on leave of absence at The National Science Foundation, Arlington, VA, USA

³³ now at Univ. of London, Queen Mary College, London, UK

³⁴ now at Northeastern University, Dana Research Center, Boston, MA, USA

³⁵ present address: Tokyo Metropolitan University of Health Sciences, Tokyo 116-8551, Japan

³⁶ also at Università del Piemonte Orientale, Novara, Italy

³⁷ now at Università di Torino, Dipartimento di Medicina Interna, Torino, Italy

³⁸ also at Łódź University, Poland

³⁹ supported by the Polish State Committee for Scientific Research, grant no. 2 P03B 07222

⁴⁰ now at The Boston Consulting Group, Warsaw, Poland

⁴¹ Łódź University, Poland

⁴² supported by German Federal Ministry for Education and Research (BMBF), POL 01/043

⁴³ on leave from MSU, partly supported by University of Wisconsin via the U.S.-Israel BSF

- ^a supported by the Natural Sciences and Engineering Research Council of Canada (NSERC)
- ^b supported by the German Federal Ministry for Education and Research (BMBF), under contract numbers HZ1GUA 2, HZ1GUB 0, HZ1PDA 5, HZ1VFA 5
- ^c supported by the MINERVA Gesellschaft für Forschung GmbH, the Israel Science Foundation, the U.S.-Israel Binational Science Foundation and the Benoziyo Center for High Energy Physics
- ^d supported by the German-Israeli Foundation and the Israel Science Foundation
- ^e supported by the Italian National Institute for Nuclear Physics (INFN)
- ^f supported by the Japanese Ministry of Education, Culture, Sports, Science and Technology (MEXT) and its grants for Scientific Research
- ^g supported by the Korean Ministry of Education and Korea Science and Engineering Foundation
- ^h supported by the Netherlands Foundation for Research on Matter (FOM)
- ⁱ supported by the Polish State Committee for Scientific Research, grant no. 620/E-77/SPUB-M/DESY/P-03/DZ 247/2000-2002
- ^j partially supported by the German Federal Ministry for Education and Research (BMBF)
- ^k supported by the Fund for Fundamental Research of Russian Ministry for Science and Education and by the German Federal Ministry for Education and Research (BMBF)
- ^l supported by the Spanish Ministry of Education and Science through funds provided by CICYT
- ^m supported by the Particle Physics and Astronomy Research Council, UK
- ⁿ supported by the US Department of Energy
- ^o supported by the US National Science Foundation
- ^p supported by the Polish State Committee for Scientific Research, grant no. 112/E-356/SPUB-M/DESY/P-03/DZ 301/2000-2002, 2 P03B 13922
- ^q supported by the Polish State Committee for Scientific Research, grant no. 115/E-343/SPUB-M/DESY/P-03/DZ 121/2001-2002, 2 P03B 07022

1 Introduction

Events with a final-state proton carrying a large fraction of the available energy but a small transverse momentum have been studied in detail in high-energy hadron-proton collisions [1]. The cross section for such leading proton events shows a peak for values of the final-state proton momentum close to the maximum kinematically allowed value, the so-called diffractive peak. For lower momenta, the cross section is lower and the fraction of events with a leading proton is approximately independent of the energy and type of the incoming particle. This characteristic behaviour has led to studies of the associated event in terms of the effective energy available for hadronisation [2, 3]. More recently, events with neutrons or protons carrying a large fraction of the proton-beam momentum have also been measured in positron-proton (e^+p) scattering at HERA [4–8].

The study of semi-inclusive rates in hadron-nucleon collisions indicates that particle production from the target nucleon is independent of the type of the incident hadron, a property known as vertex factorisation [1]. This has been studied for instance by comparing semi-inclusive rates, normalised to the respective total cross sections, for the production of particles in the fragmentation region of the target nucleon. The hadronic data [9] also show that, in the high-energy limit, the momentum distribution of the particles from the fragmentation of the target hadron is independent of the energy of the incoming particle. These characteristics have not yet been extensively studied for baryon production in electron-proton collisions.

Electroproduction of leading baryons is also interesting in other respects. The virtual photon mediating the interaction, in the reference frame in which the proton is at rest, fluctuates into a vector-meson-like object (the vector dominance model, VDM [10]). The transverse size of this projectile can be varied by changing the virtuality, Q^2 , of the photon. Real photons ($Q^2 = 0$) have hadronic size, while, as Q^2 increases, the photon size decreases. It is thus possible to experiment with a projectile of varying size. This may lead, for instance, to different absorptive rescattering of the produced baryon as Q^2 changes [11], and hence to a breaking of vertex factorisation.

Several mechanisms have been suggested to explain the hadroproduction or electroproduction of leading protons. None of them are as yet amenable to calculations based on perturbative quantum chromodynamics (pQCD). This is, in part, a consequence of the fact that the small p_T of the leading proton necessitates a non-perturbative approach. Some models [12–16] are based on the Regge formalism, with leading proton production occurring through t -channel exchanges, both isoscalar and isovector, notably Pomerons, Reggeons and pions. These exchanges mediate the interaction between the proton and the fluctuations of the virtual photon. The relative contribution of the different exchanges varies as a function of the momentum and type of the scattered baryon: for leading pro-

tons, Pomeron exchange dominates in the diffractive-peak region with Reggeon and pion exchanges contributing for lower outgoing-proton momenta. Other theoretical models retain quarks and gluons as fundamental entities, but add non-perturbative elements, such as soft-colour interactions [17]. The concept of fracture functions also offers a general theoretical framework for a QCD-based study of leading baryon physics [18].

This paper reports studies of leading proton production in e^+p collisions, $e^+p \rightarrow e^+Xp$, emphasizing the non-diffractive region. This complements the recent ZEUS study of leading neutrons [8]. High-energy protons with low transverse momentum carrying at least 60% of the incoming-proton momentum were measured in the ZEUS leading proton spectrometer (LPS) [19]. The fraction of such events with a large rapidity gap in the forward region is presented. The longitudinal- and transverse-momentum spectra are studied for different photon virtualities, from quasi-real photoproduction ($Q^2 \lesssim 0.02 \text{ GeV}^2$) to $Q^2 = 254 \text{ GeV}^2$. The dependence of the cross section for the production of leading protons on the deep inelastic scattering (DIS) variables x and Q^2 is also measured and compared to that for the inclusive reaction $e^+p \rightarrow e^+X$. The results are discussed in the context of vertex factorisation and particle-exchange models. Finally, the properties of events with a leading proton and two jets are presented.

2 Experimental set-up

The measurements were performed at the DESY ep collider HERA using the ZEUS detector. In 1994 and 1995, HERA operated at a proton energy $E_p = 820 \text{ GeV}$ and a positron energy $E_e = 27.5 \text{ GeV}$.

A detailed description of the ZEUS detector can be found elsewhere [20]. A brief outline of the components that are most relevant for this analysis is given below.

Charged particles are tracked by the central tracking detector (CTD), which operates in a magnetic field of 1.43 T provided by a thin superconducting coil. The CTD consists of 72 cylindrical drift-chamber layers, organised in nine superlayers covering the polar-angle¹ region $15^\circ < \theta < 164^\circ$. The relative transverse-momentum resolution for full-length tracks is $\sigma(p_t)/p_t = 0.0058p_t \oplus 0.0065 \oplus 0.0014/p_t$, with p_t in GeV [21].

The high-resolution uranium-scintillator calorimeter (CAL) [22] consists of three parts: the forward (FCAL), barrel (BCAL) and rear (RCAL) calorimeters. Each part is subdi-

¹ The ZEUS coordinate system is a right-handed Cartesian system, with the Z axis pointing in the proton beam direction, referred to as the “forward direction”, and the X axis pointing left towards the centre of HERA. The coordinate origin is at the nominal interaction point. The pseudorapidity is defined as $\eta = -\ln(\tan \frac{\theta}{2})$, where the polar angle, θ , is measured with respect to the proton beam direction.

vided transversely into towers and longitudinally into one electromagnetic section (EMC) and either one (in RCAL) or two (in FCAL and BCAL) hadronic sections (HAC). The relative CAL energy resolutions are $\sigma(E)/E = 0.18/\sqrt{E}$ for electrons and $\sigma(E)/E = 0.35/\sqrt{E}$ for hadrons (E in GeV).

A lead-scintillator calorimeter (LUMI- e) at $Z = -35$ m [23], with a relative energy resolution of $\sigma(E)/E = 0.18/\sqrt{E}$ (E in GeV), was used to tag events with positrons scattered through angles up to about 5 mrad, and to measure the scattered-positron energy, E'_e , over the range $7 < E'_e < 21$ GeV. These events have $Q^2 < 0.02$ GeV 2 and are hereafter referred to as the “photoproduction” sample. This sample was collected in 1994 and corresponds to an integrated luminosity of 0.898 ± 0.014 pb $^{-1}$.

Low- Q^2 events ($0.1 < Q^2 < 0.74$ GeV 2) were tagged by requiring the identification of the scattered positrons in the beam pipe calorimeter (BPC) [24–27], a tungsten-scintillator sampling calorimeter, located close to the beam pipe, 3 m downstream of the interaction point in the positron beam direction. This low- Q^2 sample, hereafter referred to as the “BPC sample”, has an integrated luminosity of 1.85 ± 0.02 pb $^{-1}$ and was collected in 1995.

For higher- Q^2 events ($Q^2 > 3$ GeV 2), the impact position on the CAL surface of the scattered positron was determined with the small-angle rear tracking detector (SRTD) [28] or the CAL. The SRTD is attached to the front face of the RCAL and consists of two planes of scintillator strips, 1 cm wide and 0.5 cm thick, arranged in orthogonal orientations. Events with $Q^2 > 3$ GeV 2 are referred to as the “DIS sample” in the following. The integrated luminosity of this sample, which was collected in 1995, is 3.38 ± 0.03 pb $^{-1}$.

The leading proton spectrometer (LPS) [19] detected charged particles scattered at small angles and carrying a substantial fraction of the incoming-proton momentum; these particles remain in the beam pipe and their trajectories were measured by a system of silicon micro-strip detectors inserted very close (typically a few mm) to the proton beam. The detectors were grouped in six stations, S1 to S6, placed along the beam-line in the direction of the proton beam, between $Z = 20$ m and $Z = 90$ m. The track deflections induced by the magnets in the proton beam-line allow a momentum analysis of the scattered proton. During data taking, the detector planes were inserted close to the beam by means of re-entrant pots and were retracted during beam dump and fill operations of the HERA machine. For the present measurements, only the stations S4, S5 and S6 were used. The intrinsic resolution is better than 1% on the longitudinal momentum and 5 MeV on the transverse momentum. The effective transverse-momentum resolution is, however, dominated by the intrinsic transverse-momentum spread of the proton beam at the interaction point, which was ≈ 40 MeV in the horizontal plane and ≈ 100 MeV in the vertical plane.

3 Kinematics and cross sections

Figure 1 illustrates semi-inclusive leading proton production in ep collisions. Four kinematic variables are needed to describe the interaction $e^+p \rightarrow e^+Xp$. They are defined in terms of the four-momenta of the incoming and outgoing positron, K and K' , and of the incoming and outgoing proton, P and P' , respectively.

Two of the kinematic variables were chosen from among the Lorentz invariants used in inclusive studies, of which only two are independent: $Q^2 = -q^2 = -(K - K')^2$, the virtuality of the exchanged photon; $x = Q^2/(2P \cdot q)$ and $y = q \cdot P/(K \cdot P) \simeq Q^2/(sx)$; and $W^2 = (P + K - K')^2 = m_p^2 + Q^2(1 - x)/x$, the square of the photon-proton centre-of-mass energy. In these equations, m_p is the mass of the proton and $\sqrt{s} = 300$ GeV is the e^+p centre-of-mass energy.

Two additional variables are required to describe the leading proton. They can be chosen as the momentum fraction carried by the outgoing proton

$$x_L = \frac{P' \cdot K}{P \cdot K}$$

and its transverse momentum with respect to the direction of the incoming proton, p_T . In terms of these variables, the square of the four-momentum transfer from the target proton is given by

$$t = (P - P')^2 \simeq -\frac{p_T^2}{x_L} - \frac{(1 - x_L)^2}{x_L} m_p^2,$$

where the second term is the minimum kinematically allowed value of $|t|$ for a given x_L . In a particle-exchange model, t is the square of the four-momentum of the exchanged particle. The p_T^2 range covered by the present data, $0 < p_T^2 < 0.5$ GeV 2 , thus translates into $0 < |t| < 0.5$ GeV 2 at $x_L = 1$ and $0.2 \lesssim |t| \lesssim 1$ GeV 2 at $x_L = 0.6$.

The differential cross section for inclusive $e^+p \rightarrow e^+X$ scattering is written in terms of the proton structure function, $F_2(x, Q^2)$, as

$$\frac{d^2\sigma_{e^+p \rightarrow e^+X}}{dxdQ^2} = \frac{4\pi\alpha^2}{xQ^4} \left(1 - y + \frac{y^2}{2}\right) F_2(x, Q^2)(1 + \Delta), \quad (1)$$

where Δ is a correction that takes account of photon radiation, Z^0 exchange, and the longitudinal structure function, F_L . In analogy with this, the differential cross section for semi-inclusive leading proton production, $e^+p \rightarrow e^+Xp$, is written as

$$\frac{d^4\sigma_{e^+p \rightarrow e^+Xp}}{dxdQ^2dx_Ldp_T^2} = \frac{4\pi\alpha^2}{xQ^4} \left(1 - y + \frac{y^2}{2}\right) F_2^{\text{LP}(4)}(x, Q^2, x_L, p_T^2)(1 + \Delta_{LP}), \quad (2)$$

where Δ_{LP} is the analogue of Δ .

3.1 Reconstruction of the kinematic variables

Three samples of data were used:

- the photoproduction sample, with the scattered positron tagged in the LUMI-*e* calorimeter;
- the BPC sample, with the scattered positron measured in the BPC;
- the DIS sample, with the scattered positron detected in the CAL.

Different methods were used for the reconstruction of the kinematic variables, Q^2 and W , for the three data sets. Tagging of the scattered positron in the LUMI-*e* calorimeter for photoproduction events does not allow the measurement of Q^2 event by event; however, the angular acceptance of the LUMI-*e* calorimeter limits the Q^2 range to the region $Q^2 < 0.02 \text{ GeV}^2$. For these events, W was measured from $W^2 = ys$, with $y = (E_e - E'_e)/E_e$, where E'_e denotes the energy of the outgoing positron. For the BPC sample, E_e and the positron scattering angle, ϑ_e , as measured in the BPC, were used (“electron method” [24]) to determine Q^2 , W , x and y . For the DIS sample, these variables were reconstructed using the double angle method [29].

For the reconstruction of the hadronic final state, X , the energy deposits in the CAL and the track momenta measured in the CTD for the charged particles were clustered into energy-flow objects (EFOs) which are assumed to correspond to particles and are assigned the pion mass [30, 31]. The EFOs were used to reconstruct the mass, M_X , of the hadronic final state contained in the central detector. Using the EFOs, the y variable was also reconstructed with the Jacquet-Blondel method [32], which uses information from the hadronic final state to reconstruct the event kinematics, and was denoted by y_{JB} . Furthermore, the variable

$$\delta = \sum_i (E_i - p_{Z,i}) + E'_e (1 - \cos \vartheta_e)$$

was evaluated, where \sum_i denotes a sum over all EFOs, excluding those assigned to the scattered positron, and E_i and $p_{Z,i}$ are the energy and the longitudinal momentum of each EFO, respectively. For perfect resolution and fully contained events, energy and momentum conservation constrain δ to be twice the positron beam energy. The angle of the hadronic final state (as measured in the ZEUS central detector) with respect to the incoming-proton direction was evaluated from

$$\cos \gamma_h = \frac{(\sum_i p_{T,i})^2 - (\sum_i (E_i - p_{z,i}))^2}{(\sum_i p_{T,i})^2 + (\sum_i (E_i - p_{z,i}))^2},$$

where the sums \sum_i run over all EFOs excluding those assigned to the scattered positron.

The modulus of the momentum of the scattered proton, p' , was measured in the LPS, along with its component perpendicular to the mean proton beam direction, p_T . The variable x_L was evaluated as $x_L = p'/E_p$. The mean direction of the incoming proton beam was determined for each proton fill of HERA using the reaction $ep \rightarrow e\rho^0 p$ at $Q^2 \approx 0$ [19].

In the following, the term “leading proton” is used to indicate a positively charged particle detected in the LPS. In the present measurement, x_L is restricted to values larger than 0.6. Charged-particle production measured at the ISR [2, 33] shows that the pion-to-proton ratio at $x_L = 0.6$ is about 10% and falls rapidly for increasing values of x_L .

4 Event selection

Photoproduction events were selected at the trigger level by requiring a coincidence between an energy deposit of at least 5 GeV in the LUMI- e and of at least 464 MeV in the RCAL (excluding the towers immediately adjacent to the beam-pipe) or at least 1250 MeV (including those towers). This requirement helps to suppress the background from bremsstrahlung events ($ep \rightarrow e\gamma p$) characterised by having a scattered positron in the LUMI- e and no activity in the rest of the detector. The BPC and DIS events were triggered by requiring the presence of a scattered positron in the BPC and the CAL, respectively. No requirement was imposed on the final-state proton at the trigger level.

Events were selected offline in three steps: first inclusive events with the scattered positron in the LUMI- e , the BPC or the CAL were selected; then, a track in the LPS was required; finally a search for jets was carried out in the hadronic final state, X . The details of the selection procedure are presented in the rest of this section. The following requirements were imposed for all samples:

- the Z coordinate of the reconstructed vertex, if measured, in the range $-50 < Z < 50$ cm;
- the timing of the interaction, as measured by the CAL, consistent with the timing of an e^+p bunch crossing.

For the BPC and DIS samples, the requirement $35 < \delta < 65$ GeV was also imposed in order to reduce the photoproduction background and to minimise the effect of the radiative corrections.

The photoproduction sample [34] was selected by requiring that a positron be measured in the LUMI- e with energy in the range $12 < E'_e < 18$ GeV, corresponding to $176 < W < 225$ GeV. Overlay events, in which some activity in the RCAL accidentally overlaps

with the scattered positron of a bremsstrahlung event ($ep \rightarrow e\gamma p$) in the LUMI- e , were subtracted as discussed in an earlier study [35]. The subtraction was less than 3%.

The BPC sample [24, 36] was selected by requiring a scattered positron measured in the BPC with $E'_e > 7$ GeV and a photon virtuality in the range $0.1 < Q^2 < 0.74$ GeV 2 . In addition, the requirement $0.08 < y < 0.74$ was imposed, which corresponds to $85 < W < 258$ GeV. Finally, $y_{JB} > 0.05$ was required, thus ensuring hadronic activity away from the forward direction and reducing the migration of events from low y , where the resolution of the electron method is poor.

In the DIS analysis [34, 36], a scattered positron with energy $E'_e > 10$ GeV was required in the CAL; the photon virtuality was restricted to the interval $3 < Q^2 < 254$ GeV 2 and W to the region $45 < W < 225$ GeV. Finally, the condition $y_{JB} > 0.03$ was imposed.

The total number of events thus selected was approximately 94 000 for the photoproduction sample, 50 000 for the BPC sample and 386 000 for the DIS sample.

Next, high-momentum protons in the LPS were selected by requiring:

- one track in the LPS with $p_T^2 < 0.5$ GeV 2 and $0.6 < x_L < 1.02$. For $x_L > 0.97$, a lower bound on p_T^2 was also imposed: $p_T^2 > 0.073$ GeV 2 . For the 1994 data, the p_T^2 range was restricted to $p_T^2 < 0.04$ GeV 2 . The p_T^2 cuts and the lower limit on x_L restrict the data to a region of well understood acceptance;
- no candidate track was accepted if, at any point, the minimum distance of approach to the beam pipe, Δ_{pipe} , was less than 0.4 mm (0.5 mm for the 1994 data). This cut reduced the sensitivity of the acceptance to the uncertainty on the location of the beam-pipe apertures;
- events in which the reconstructed proton track passed closer than a distance $\Delta_{\text{plane}} = 0.2$ mm to the edge of any LPS detector were rejected. This ensured that the track was well within the active region of the detectors;
- the total $E + p_Z$ of the event was required to be smaller than 1655 GeV. For fully contained events, this quantity should be equal to $2E_p = 1640$ GeV. This cut rejects random overlays of a beam-halo proton and an event satisfying the trigger and selection cuts applied to the non-LPS variables;
- for $x_L > 0.97$, $M_X > 2$ GeV was required, where M_X is the reconstructed hadronic mass in the CAL. This rejects contributions from exclusive production of low-mass vector mesons, which have Q^2 and t dependences different from those of the inclusive events [37].

After this selection, the total number of events with a good LPS track was 1834 for the photoproduction sample, 1697 for the BPC sample and 13335 for the DIS sample.

Finally, a search was performed for jets in the hadronic final state [38]. Because of the limited statistics of the photoproduction and BPC samples, the search was limited to the DIS data. The jets were reconstructed using the k_T algorithm [39], requiring a jet transverse energy $E_T > 4$ GeV in the γ^*p centre-of-mass system and a jet pseudorapidity, in the laboratory frame, in the range $-2 < \eta^{\text{jet}} < 2.2$. A sample of 225 events with exactly two jets was selected.

5 Monte Carlo simulation

Several Monte Carlo (MC) generators were used to determine the acceptance of the apparatus for events with a leading proton. The EPSOFT2.0 Monte Carlo [40–42] was used for the BPC data. This generator simulates diffractive processes with dissociation of the virtual photon, as well as non-diffractive processes. Vertex factorisation is assumed. The HERACLES4.6 Monte Carlo [43], which simulates initial- and final-state QED radiation, is interfaced to EPSOFT. Samples of DIS events were simulated with RAPGAP [44, 45] version 2.06/06, which incorporates meson and Pomeron exchange; it also assumes vertex factorisation. QED radiation was also simulated using HERACLES. Weights were assigned to the events generated with EPSOFT and RAPGAP such that the reconstructed proton x_L and p_T^2 spectra agreed with the data. For the photoproduction data, and for systematic studies, events that only contain a proton with distributions in x_L and p_T^2 tuned to those of the data were generated. This simulation produced the same results for the LPS acceptance as EPSOFT and RAPGAP.

All generated events were passed through the trigger-simulation package and the standard ZEUS detector simulation, based on the GEANT 3.13 program [46]. The simulation includes the geometry of the beam-pipe apertures, the HERA magnets and their magnetic fields. The spread of the interaction-vertex position was also simulated, as were the proton-beam angle with respect to the nominal direction and its dispersion at the interaction point. The simulated events were then passed through the same reconstruction and analysis programs as the data.

Figures 2a)-c) compare the distributions of the reconstructed variables E'_e , ϑ_e , and y_{JB} in events generated with EPSOFT with those for the BPC data. The agreement between the data and the simulated distributions is good. A similarly good description of the DIS data by RAPGAP is shown in Figs. 2d)-f) for the variables E'_e , ϑ_e and γ_h .

The agreement between the data and the MC simulation of the leading-proton variables is also good for all three samples. As an example, the distributions for the reconstructed EPSOFT events as a function of x_L , p_T^2 , Δ_{pipe} and Δ_{plane} are compared with those of the BPC data in Fig. 3.

6 Acceptance

Figure 4 shows the ranges of p_X and p_Y accessed by the LPS for six values of x_L , using the coincidence of any two of the S4, S5 and S6 stations. Here, p_X and p_Y are the X and Y components of the scattered-proton momentum. The region covered is determined by the beam-pipe apertures, the shape of the sensitive region of the LPS detectors and the magnet strengths; it is limited to $x_L \gtrsim 0.5$ and $p_T^2 = p_X^2 + p_Y^2 \lesssim 0.7$ GeV 2 . Integrated over the falling p_T^2 distribution, the LPS geometrical acceptance reaches a maximum for x_L in the range 0.8 to 0.9.

The acceptance was computed as the ratio of the number of reconstructed events in a bin of a given variable to the number of generated events in that bin. The acceptance thus includes the effects of the geometrical acceptance of the apparatus, its efficiency and resolution, as well as the event selection and reconstruction efficiencies. Values of the acceptance are given in Section 8.

7 Systematic uncertainties

The systematic uncertainties were obtained by modifying the requirements and the analysis procedures as listed below:

- the sensitivity to the selection of the proton track was studied by the following procedure [19]:
 - the track-selection requirements were varied. In particular, the minimum-allowed values of Δ_{pipe} were changed from 0.2 to 0.6 mm and the minimum value of Δ_{plane} was varied from 0.1 to 0.3 mm;
 - the positions of some of the elements of the proton beam-line were varied within their uncertainties. This is particularly relevant at low x_L , where the proton momentum is significantly lower than that of the $x_L \approx 1$ protons used in the LPS alignment procedure;
 - the LPS detector positions varied slightly from fill to fill in the 94 sample. The small deviations of the acceptance implied by these movements were estimated by dividing the data into a “low acceptance” and a “high acceptance” sample, depending on the positions of the LPS stations;
- the sensitivity to the remaining selection cuts was also investigated:
 - for the inclusive photoproduction sample, the selection cuts were tightened: the E'_e range was restricted to $13 < E'_e < 16$ GeV, corresponding to $195 < W < 215$ GeV

and the minimum energy deposition in the RCAL was raised to 2 GeV. In addition, the correction for the bremsstrahlung background was removed [35];

- for the BPC sample, the BPC energy scale was varied by $\pm 1\%$ and the sizes of the parameters in the BPC energy calibration were changed within their uncertainties [24]. The selection limits on the positron-candidate shower width were also varied [24];
- for the DIS sample, the positron-selection procedure was varied. The cut on the scattered-positron energy was changed to 8 GeV and 12 GeV and the size of the fiducial region for the impact position of the scattered positron in the SRTD was raised by ± 0.5 cm in both X and Y ;
- for both the BPC and the DIS samples, the lower limit on δ was varied between 32 and 38 GeV and the upper limit between 60 and 68 GeV; the cut on y_{JB} was varied by ± 0.01 ;
- the allowed range of values for the Z coordinate of the vertex was restricted to $-40 < Z < 40$ cm. The effect of removing the vertex requirement was also studied;
- in addition, for the jet studies, the minimum jet energy was varied between 3.8 and 4.2 GeV, and the upper limit on η^{jet} was varied between 2 and 2.4.

The total systematic uncertainty on the cross sections, obtained by summing all the above contributions in quadrature, totalled about $\pm 20\%$ at $x_L \approx 0.65$, decreasing to $\pm(10\text{-}15)\%$ for $x_L \gtrsim 0.75$. The dominant contributions are those related to the track-selection requirements in the LPS.

8 The ratio method

In the following, several results are presented in terms of the ratios, $r^{\text{LP}(2)}$ and $r^{\text{LP}(3)}$, of the cross section for production of leading protons to the cross section for inclusive e^+p scattering; these ratios are evaluated in bins of x and Q^2 ($r^{\text{LP}(2)}$), or in bins of x , Q^2 and x_L ($r^{\text{LP}(3)}$). They are obtained from the measured fraction of the events, in a given bin, that have a leading proton, N^{LP}/N . In this fraction, the acceptance corrections related to the positron selection procedure cancel, and so do the corresponding systematic uncertainties. The only remaining correction to apply is that for the LPS acceptance, ϵ_{LPS} .

The ratio $r^{\text{LP}(2)}$ was thus obtained as

$$r^{\text{LP}(2)}(x, Q^2) = \frac{N^{\text{LP}}(x, Q^2)}{N(x, Q^2)} \frac{1}{\epsilon_{\text{LPS}}}.$$

Averaged over the region $0.6 < x_L < 0.97$ and $p_T^2 < 0.5 \text{ GeV}^2$, ϵ_{LPS} is approximately 23%; over the region $0.6 < x_L < 0.97$ and $p_T^2 < 0.04 \text{ GeV}^2$, $\epsilon_{\text{LPS}} \approx 51\%$.

From Eqs. (1) and (2), it is apparent that the cross section ratio $r^{\text{LP}(2)}$ is also equal to the ratio of the proton tagged and inclusive structure functions:

$$r^{\text{LP}(2)}(x, Q^2) = \frac{\bar{F}_2^{\text{LP}(2)}(x, Q^2)}{F_2(x, Q^2)}, \quad (3)$$

where $\bar{F}_2^{\text{LP}(2)}$ is obtained from $F_2^{\text{LP}(4)}$ by integration over the measured x_L and p_T^2 ranges:

$$\bar{F}_2^{\text{LP}(2)}(x, Q^2) = \int_0^{p_T^2 \text{max}} dp_T^2 \int_{0.6}^{0.97} dx_L F_2^{\text{LP}(4)}(x, Q^2, x_L, p_T^2).$$

The radiative corrections and the contributions from F_L are assumed to be the same for the inclusive and the proton-tagged reactions.

The ratio $r^{\text{LP}(3)}(x, Q^2, x_L)$ is defined in analogy to $r^{\text{LP}(2)}(x, Q^2)$:

$$r^{\text{LP}(3)}(x, Q^2, x_L) = \frac{N^{\text{LP}}(x, Q^2, x_L)}{N(x, Q^2)} \frac{1}{\epsilon_{LPS}(x_L) \Delta x_L}, \quad (4)$$

where Δx_L indicates the size of the x_L bins. In analogy with Eq. (3),

$$r^{\text{LP}(3)}(x, Q^2, x_L) = \frac{\bar{F}_2^{\text{LP}(3)}(x, Q^2, x_L)}{F_2(x, Q^2)}, \quad (5)$$

where $\bar{F}_2^{\text{LP}(3)}(x, Q^2, x_L)$ differs from $\bar{F}_2^{\text{LP}(2)}(x, Q^2)$ in that no integration over x_L is performed.

The ratios $r^{\text{LP}(2)}$ and $r^{\text{LP}(3)}$ can also be interpreted in terms of the virtual photon-proton cross section for the process $\gamma^* p \rightarrow X p$ and the total virtual photon-proton cross section, σ_{tot} . For example, the ratio $r^{\text{LP}(3)}$ can be written as

$$r^{\text{LP}(3)}(x, Q^2, x_L) = \frac{1}{\sigma_{\text{tot}}} \int_0^{p_T^2 \text{max}} dp_T^2 \frac{d^2 \sigma_{\gamma^* p \rightarrow X p}}{dx_L dp_T^2} = \frac{1}{\sigma_{\text{tot}}} \frac{d \sigma_{\gamma^* p \rightarrow X p}}{dx_L},$$

where the virtual photon-proton cross section, $d^2 \sigma_{\gamma^* p \rightarrow X p} / dx_L dp_T^2$, is related to the positron-proton cross section, $d^4 \sigma_{e^+ p \rightarrow e^+ X p} / dQ^2 dx_L dp_T^2$, by

$$\frac{d^4 \sigma_{e^+ p \rightarrow e^+ X p}}{dQ^2 dx_L dp_T^2} = \Gamma \frac{d^2 \sigma_{\gamma^* p \rightarrow X p}}{dx_L dp_T^2},$$

where $\Gamma = (\alpha / x Q^2 \pi) [1 + (1 - y^2)]$, is the photon flux factor and α is the fine-structure constant.

9 Models

The data were tested against the hypothesis of vertex factorisation, a very general feature of hadron-hadron interactions [1] which relates reactions with different beam particles to their respective total cross sections. In particular, in the reaction $\gamma^*p \rightarrow Xp$, the γ^*X and $p-p$ vertices factorise if the amplitude for the reaction can be written as the product of two vertex functions, $G_{\gamma^*X}(x, Q^2)$ and $G_{pp}(x_L, p_T^2)$. In this case, the cross section as a function of the lepton variables x and Q^2 should be independent of the baryon variables x_L and p_T^2 , and *vice versa*.

The data were also compared to the following specific models:

- the LUND string-fragmentation model as implemented in JETSET [47] and used in DJANGO [48], in which leading baryons originate from the hadronisation of the target;
- the soft-colour-interaction model (SCI) [17], as implemented in LEPTO 6.5 [49], where leading protons are obtained from standard DIS events by means of a non-perturbative redistribution of colour among the fragmenting partons;
- the Regge model of Szczerba et al. [16], which assumes a superposition of Pomeron, Reggeon and pion exchanges;
- the QCD-inspired model of Durães et al. [50], developed in the framework of the interacting-gluon model [51], which assumes that high-energy hadron-hadron collisions are dominated by multiple incoherent gluon-gluon interactions. The valence quarks that do not take part in the interaction give rise to the leading baryons. The extension to ep collisions is made in the VDM framework.

10 Results

10.1 Leading proton events with a forward large rapidity gap

Some indication of the production mechanism of leading protons can be obtained from the rapidity distribution of the hadronic final-state particles. In particular, events of diffractive origin, i.e. due to Pomeron exchange, are characterised by a gap in the rapidity distribution in the forward direction.

Figure 5a) shows the distribution of the DIS events in the (η_{\max}, x_L) plane, where η_{\max} is the pseudorapidity of the most-forward energy deposit of at least 400 MeV in the CAL. The accumulation of events at $x_L \approx 1$, which mostly have $\eta_{\max} < 2.5$, is due to diffractive events [52], $e^+p \rightarrow e^+Xp$, in which the final-state proton remains intact and carries approximately the same momentum as the incoming proton. Events with

$\eta_{\max} < 2.5$ and $x_L \lesssim 0.97$ are ascribed to double diffractive dissociation, $e^+p \rightarrow e^+XN$, where the proton dissociates into the state N , with mass M_N . Although N is produced at $x_L \simeq 1$, the proton from the decay of N has a lower value of x_L . When both M_N and M_X are small, the systems X and N are separated by a large gap in pseudorapidity. If $M_N < 4.5$ GeV, only the proton from the system N is measured, while the other particles escape undetected down the beam pipe. The topology of a doubly dissociative event is thus characterised by a rapidity gap in the forward region in conjunction with a low- x_L proton.

To select a sample of diffractive events, the requirement $\eta_{\max} < 2.5$ was imposed. Figure 5b) shows the fraction of BPC and DIS events with a leading proton that also have $\eta_{\max} < 2.5$ (see also Table 1). Events with a large rapidity gap dominate for $x_L \approx 1$. For $0.6 < x_L < 0.97$, the fraction of leading proton events with a large rapidity gap is less than 10% in any given bin, and is only weakly dependent on Q^2 and x_L . This result, which indicates that diffraction is not the main mechanism responsible for production of leading protons in this region, is consistent with the predictions of the Regge-based models [16, 53].

10.2 Momentum spectra of leading protons

10.2.1 Longitudinal-momentum spectra

The normalised cross-section $r^{\text{LP}(3)} = (1/\sigma_{\text{tot}}) \cdot d\sigma_{\gamma^*p \rightarrow Xp}/dx_L$ for the reaction $e^+p \rightarrow e^+Xp$ with a leading proton having $x_L > 0.6$ and $p_T^2 < 0.5$ GeV 2 is shown in Fig. 6 and given in Table 2 for the BPC sample, integrated over the range $0.1 < Q^2 < 0.74$ GeV 2 , $85 < W < 258$ GeV, $1.5 \times 10^{-6} < x < 1.0 \times 10^{-4}$, and for the DIS sample, integrated over the region $3 < Q^2 < 254$ GeV 2 , $45 < W < 225$ GeV, $1.2 \times 10^{-4} < x < 4 \times 10^{-2}$. These results are compared with those from the reaction $pp \rightarrow pX$ at $\sqrt{s} = 19.6$ GeV [54], integrated over the same p_T^2 region and normalised to the corresponding inelastic cross section. For $x_L \lesssim 0.9$, the fraction of events with a leading proton is consistent for the pp and γ^*p data sets, in accord with vertex factorisation. A dependence on the centre-of-mass energy is apparent for $x_L > 0.9$, as expected from Regge parametrisations of the $pp \rightarrow pX$ data [55, 56].

Figure 7 and Table 3 present the photoproduction, BPC and DIS data for the lower p_T^2 region, $p_T^2 < 0.04$ GeV 2 and $0.6 < x_L < 0.95$, where the upper cut on x_L , which removes the diffractive events, is set by the LPS acceptance for this p_T^2 range. The fraction of events with a leading proton is approximately the same in all three regimes. The pp data [54] for $p_T^2 < 0.05$ GeV 2 again agree with the ep data for $x_L \lesssim 0.9$. The present

photoproduction results, however, are significantly higher than those found by H1 [7] in similar ranges of Q^2 , W and p_T^2 .

Figure 8 compares the DIS data to the specific models of Section 9. The standard DIS Monte Carlo generator DJANGO [48] predicts a stronger decrease of the cross section with x_L than that observed and, in addition, has no diffractive peak. It also substantially underestimates the rate of leading proton production in the measured x_L range. The SCI model [17], as implemented in LEPTO6.5 [49], also falls below the data, even though it generates a larger number of leading protons than DJANGO and has a peak at $x_L = 1$. These two models are ruled out by the data.

The QCD-inspired model of Durães et al. [50, 57] is in better agreement with the data, but is too low in the diffractive peak region. Nevertheless, the similarity to the data is remarkable, given the small number of free parameters in the model.

The Regge-based calculation of Szczerba et al. [16] agrees with the data, although it is somewhat too low at small values of x_L . In this approach, leading proton production for $0.6 < x_L < 0.9$ is dominated by isoscalar Reggeon exchange; diffractive processes, due to Pomeron exchange, become increasingly important as x_L approaches unity. The contribution of pion exchange, including the production of Δ baryons, is also evaluated. The normalisation of the Reggeon contribution has a large theoretical uncertainty [16, 58] and the present data suggest that this contribution should be increased with respect to the assumption made by Szczerba et al. [16].

10.2.2 Transverse-momentum spectra

The cross-sections $d\sigma_{\gamma^* p \rightarrow X p} / dp_T^2$ are shown in Fig. 9 for the BPC sample integrated over the range $0.1 < Q^2 < 0.74$ GeV 2 , $85 < W < 258$ GeV, $1.5 \times 10^{-6} < x < 1.0 \times 10^{-4}$ for different x_L selections. Similar distributions for the DIS sample are shown in Fig. 10, integrated over the region $3 < Q^2 < 254$ GeV 2 , $45 < W < 225$ GeV, $1.2 \times 10^{-4} < x < 4 \times 10^{-2}$. In all regions, the form $d\sigma_{\gamma^* p \rightarrow X p} / dp_T^2 = Ae^{-bp_T^2}$ fits satisfactorily the data. The values of the slope-parameters b obtained for each x_L bin are, within uncertainties, independent of x_L , as shown in Fig. 11 (see also Table 4).

The BPC and DIS data together indicate that b is independent of Q^2 and x_L . The mean value of b for the BPC data is $\langle b \rangle = 6.6 \pm 0.6$ (stat.) ± 0.8 (syst.) GeV $^{-2}$ and $\langle b \rangle = 6.9 \pm 0.2$ (stat.) ± 0.8 (syst.) GeV $^{-2}$ for the DIS data for $0.6 < x_L < 0.97$. Also plotted in Fig. 11a) is the result obtained for diffractive photoproduction [59], which is consistent with the values found at higher Q^2 . In addition, the present results are compatible with the $pp \rightarrow pX$ data [54], also shown in Fig. 11a). This, together with the fact that b is approximately Q^2 -independent, provides additional support for vertex

factorisation.

The predictions of Szczurek et al. [16] are in accord with the transverse-momentum data, as shown in Fig. 11b). In this model, no Q^2 dependence is expected for b [60]. The DJANGO program (not shown) has an effective slope $b \approx 4 \text{ GeV}^{-2}$. LEPTO6.5 (also not shown) has $b \approx 3.5 \text{ GeV}^{-2}$. Both are independent of x_L and significantly below the values measured. The model of Durães et al. [50] does not make explicit predictions for the transverse-momentum distribution.

10.3 The proton-tagged structure-function \bar{F}_2^{LP}

The acceptance-corrected fraction of events with a leading proton is used to measure the proton-tagged structure-function \bar{F}_2^{LP} , as discussed in Section 8. To select a predominantly non-diffractive sample, the cut $x_L < 0.97$ was imposed.

Figures 12 and 13 show $r^{\text{LP}(3)}(x, Q^2, x_L)$, determined using Eq. (4), for the BPC and DIS samples, respectively, in several x and Q^2 bins for $p_T^2 < 0.5 \text{ GeV}^2$. The data are also given in Tables 5-7. Only a weak dependence on x and Q^2 is apparent, indicating that $\bar{F}_2^{\text{LP}(3)}$ has approximately the same x and Q^2 dependence as $F_2(x, Q^2)$. The data exhibit a weak x_L dependence, as already seen in Fig. 6. Figure 14 shows $r^{\text{LP}(2)}$ for fixed Q^2 values as a function of x ; the results again have little x dependence (see also Table 8).

Figure 15a) and Table 9 present the BPC and DIS data for $0.6 < x_L < 0.97$ and $p_T^2 < 0.5 \text{ GeV}^2$, averaged over x for different Q^2 ranges, $\langle r^{\text{LP}(2)}(Q^2) \rangle$. The leading proton yield increases by approximately 20%, from $\langle r^{\text{LP}(2)} \rangle \approx 0.12$ to $\langle r^{\text{LP}(2)} \rangle \approx 0.15$, when Q^2 varies from $\approx 0.25 \text{ GeV}^2$ (the average value of Q^2 for the BPC sample) to 100 GeV^2 , indicating a modest but definite breakdown of vertex factorisation. Figure 15b) and Table 10 present the points of Fig. 15a) normalised to $\langle r^{\text{LP}(2)}(Q^2 = 0.25 \text{ GeV}^2) \rangle$. The results for the restricted p_T^2 range, $p_T^2 < 0.04 \text{ GeV}^2$, are also shown. The breaking of vertex factorisation is approximately the same for $p_T^2 < 0.5 \text{ GeV}^2$ and for $p_T^2 < 0.04 \text{ GeV}^2$. An effect of similar size was measured for leading neutron production [8]; the corresponding data, normalised to the value at $Q^2 = 0.25 \text{ GeV}^2$, are also shown in Fig. 15b). The neutron data are measured for scattering angles less than 0.8 mrad, corresponding to $p_T^2 < 0.43 \cdot x_L^2 \text{ GeV}^2$.

This Q^2 dependence of the proton yield can be qualitatively ascribed to absorptive effects in the $\gamma^* p$ system [11]. The transverse size of the virtual photon decreases with increasing Q^2 , reducing the likelihood that the produced baryon rescatters on the hadronic component of the virtual photon.

The data of Fig. 14 are presented in Fig. 16 in terms of $\bar{F}_2^{\text{LP}(2)}$, obtained by multiplying $r^{\text{LP}(2)}$ by F_2 . For the BPC region, a parameterisation of the ZEUS F_2 results [25] was

used. For the DIS region, the parameterisation of Botje [61] was used. Since $r^{\text{LP}(2)}$ is approximately independent of Q^2 and x , $\bar{F}_2^{\text{LP}(2)}$ is approximately proportional to F_2 . As indicated in the figure, the proportionality constant between $\bar{F}_2^{\text{LP}(2)}$ and F_2 is $\langle r^{\text{LP}(2)} \rangle \approx 0.13$.

The H1 collaboration has published [5] a study of leading proton production for $p_T^2 < 0.04 \text{ GeV}^2$, $0.7 < x_L < 0.9$, $2 < Q^2 < 50 \text{ GeV}^2$ and $6 \times 10^{-5} < x < 6 \times 10^{-3}$. The present analysis was repeated in the region of overlap with the H1 data set. A comparison of the H1 and ZEUS results is presented in Fig. 17. The agreement is good.

10.4 Leading protons with associated dijet production

The ratio $r_{\text{LP}}^{\text{jet}}$ of the yield of leading proton DIS events with associated dijet production to the inclusive yield of leading proton events is presented as a function of x_L and p_T^2 in Fig. 18 and Tables 13-14. The LPS acceptance, as well as the scattered positron acceptance, cancels in this ratio. The data are shown for the range $0.6 < x_L < 0.97$ and $p_T^2 < 0.5 \text{ GeV}^2$. No significant deviation from a flat behaviour is seen as a function of x_L , although there is some p_T^2 dependence. The results of this exploratory study thus suggest that the longitudinal- and transverse-momentum distributions of the leading proton are largely insensitive to the presence of a second hard scale, given by the transverse energy of the jets.

Figure 19 and Tables 15-17 present the fraction of the dijet events with a leading proton, $r_{\text{jet}}^{\text{LP}}$, plotted as a function of E_T , x and Q^2 . In this case, all corrections cancel with the exception of that due to the LPS acceptance, which is, however, independent of E_T , Q^2 and x . The ratio is approximately independent of these variables and its value is consistent with that of $r^{\text{LP}(2)}$. This suggests that the E_T , Q^2 and x dependences of the dijet cross section are unaffected by the requirement of a leading proton, and that the fraction of dijet events with a leading proton is the same as the fraction of inclusive events with a leading proton.

10.5 Summary

Events of the type $e^+p \rightarrow e^+Xp$ with a final-state proton with $x_L > 0.6$ have been studied in e^+p collisions at HERA. The analyses used a photoproduction sample ($Q^2 < 0.02 \text{ GeV}^2$), a low- Q^2 sample ($0.1 < Q^2 < 0.74 \text{ GeV}^2$) and a DIS sample ($3 < Q^2 < 254 \text{ GeV}^2$).

For events with a leading proton in the range $0.6 < x_L < 0.97$ and $p_T^2 < 0.5 \text{ GeV}^2$, the main features of the data can be summarised as follows:

- less than 10% of the leading proton events in any given x_L bin exhibit a large rapidity gap ($\eta_{\max} < 2.5$), indicating that diffraction is not the main mechanism responsible for the production of leading protons in this region;
- the proton x_L spectrum is only a weak function of x_L for $x_L \lesssim 0.97$;
- the p_T^2 dependence of the cross section is well described by an exponential function, with a slope approximately independent of x_L and Q^2 , $b \approx 7 \text{ GeV}^{-2}$. The slope is also consistent with the value measured for pp collisions;
- the x and Q^2 dependence of the semi-inclusive structure function, F_2^{LP} , is similar to that of F_2 , independently of x_L . However, F_2^{LP} grows with Q^2 slightly faster than F_2 , resulting in a yield of leading protons about 20% larger at $Q^2 = 100 \text{ GeV}^2$ than at $Q^2 \approx 0$. A similar effect was observed for leading neutron production;
- the shapes of the x_L and p_T^2 spectra are largely unaffected by requiring two jets within the hadronic final state X . The Q^2 , x and E_T dependences of the dijet cross section are also broadly consistent for leading proton events and inclusive events.

The main features of the data are reproduced by a Regge model assuming a superposition of Pomeron, Reggeon and pion trajectories. The DJANGO and SCI models are ruled out by the data.

For $0.6 < x_L < 0.9$, the proton spectrum for (virtual-) photon-proton collisions is consistent with the results found in proton-proton reactions at lower centre-of-mass energy. The fraction of the events with a leading proton is approximately the same for the γ^*p and pp data, in agreement with vertex factorisation.

In the x_L region explored, a modest violation of vertex factorisation is observed. Nevertheless, the results of this paper indicate that the properties of the final-state proton are largely independent of those of the virtual photon.

Acknowledgements

We thank the DESY Directorate for their encouragement, and gratefully acknowledge the support of the DESY computing and network services. We are specially grateful to the HERA machine group: collaboration with them was crucial to the successful installation and operation of the leading proton spectrometer. The design, construction and installation of the ZEUS detector have been made possible by the ingenuity and effort of many people from DESY and home institutes who are not listed as authors. Finally, it is a pleasure to thank F.S. Navarra, N.N. Nikolaev and A. Szczurek for many useful discussions.

References

- [1] See e.g.:
G. Alberi and G. Goggi, Phys. Rep. **74**, 1 (1981);
K. Goulianos, Phys. Rep. **102**, 169 (1983), and references therein.
- [2] M. Basile et al., Nuovo Cimento **66A**, 129 (1981).
- [3] M. Basile et al., Lettere al Nuovo Cimento **32**, 321 (1981);
V.N. Gribov et al., *The creation of QCD and the effective energy*, L.N. Lipatov (ed.),
World Scientific Series in 20th Century Physics, Vol. 25, World Scientific, Singapore
(2001).
- [4] ZEUS Collab., M. Derrick et al., Phys. Lett. **B 384**, 388 (1996).
- [5] H1 Collab., C. Adloff et al., Eur. Phys. J. **C 6**, 587 (1999).
- [6] ZEUS Collab., J. Breitweg et al., Nucl. Phys. **B 593**, 1 (2000).
- [7] H1 Collab., C. Adloff et al., Nucl. Phys. **B 619**, 3 (2001).
- [8] ZEUS Collab., S. Chekanov et al., Nucl. Phys. **B 637**, 3 (2002).
- [9] G. Bellettini et al., Phys. Lett. **B 45**, 69 (1973);
G.J. Alner et al., Z. Phys. **C 33**, 1 (1986).
- [10] J.J. Sakurai, Ann. Phys. (NY) **11**, 1 (1960);
J.J. Sakurai, Phys. Rev. Lett. **22**, 981 (1969).
- [11] N.N. Nikolaev, J. Speth and B.G. Zakharov, hep-ph/9708290 (1997);
U. D'Alesio and H.J. Pirner, Eur. Phys. J. **A 7**, 109 (2000).
- [12] J. D. Sullivan, Phys. Rev. **D 5**, 1732 (1972).
- [13] R. Zoller, Z. Phys. **C 53**, 443 (1992).
- [14] H. Holtmann et al., Phys. Lett. **B 338**, 363 (1994).
- [15] B. Kopeliovich, B. Povh and I. Potashnikova, Z. Phys. **C 73**, 125 (1996).
- [16] A. Szczurek, N.N. Nikolaev and J. Speth, Phys. Lett. **B 428**, 383 (1998).
- [17] A. Edin, G. Ingelman and J. Rathsman, Phys. Lett. **B 366**, 371 (1996).
- [18] L. Trentadue and G. Veneziano, Phys. Lett. **B 323**, 210 (1994);
D. Graudenz, Nucl. Phys. **B 432**, 351 (1994);
L. Trentadue, Nucl. Phys. Proc. Suppl. **39 BC**, 50 (1995);
L. Trentadue, Nucl. Phys. Proc. Suppl. **64**, 152 (1998).
For applications to HERA see also:
D. de Florian and R. Sassot, Phys. Rev. **D 56**, 426 (1997) and Phys. Rev. **D 58**,
054003 (1998).

- [19] ZEUS Collab., M. Derrick et al., *Z. Phys. C* **73**, 253 (1997).
- [20] ZEUS Collab., U. Holm (ed.), *The ZEUS Detector*, Status Report (unpublished) DESY, 1993, available on <http://www-zeus.desy.de/bluebook/bluebook.html>.
- [21] N. Harnew et al., *Nucl. Instr. and Meth. A* **279**, 290 (1989);
B. Foster et al., *Nucl. Phys. Proc. Suppl. B* **32**, 181 (1993);
B. Foster et al., *Nucl. Instr. and Meth. A* **338**, 254 (1994).
- [22] M. Derrick et al., *Nucl. Instr. and Meth. A* **309**, 77 (1991);
A. Andresen et al., *Nucl. Instr. and Meth. A* **309**, 101 (1991);
A. Caldwell et al., *Nucl. Instr. and Meth. A* **321**, 356 (1992);
A. Bernstein et al., *Nucl. Instr. and Meth. A* **336**, 23 (1993).
- [23] J. Andruszków et al., Report DESY-92-066, DESY, 1992;
ZEUS Collab., M. Derrick et al., *Z. Phys. C* **63**, 391 (1994);
J. Andruszków et al., *Acta Phys. Pol. B* **32**, 2025 (2001).
- [24] ZEUS Collab., J. Breitweg et al., *Phys. Lett. B* **407**, 432 (1997).
- [25] ZEUS Collab., J. Breitweg et al., *Phys. Lett. B* **487**, 53 (2000).
- [26] B. Surrow, Ph.D. thesis, University of Hamburg (1998), Report DESY-THESIS-1998-004.
- [27] T. Monteiro, Ph.D. thesis, University of Hamburg (1998), Report DESY-THESIS-1998-027.
- [28] A. Bamberger et al., *Nucl. Instr. and Meth. A* **401**, 63 (1997).
- [29] S. Bentvelsen, J. Engelen and P. Kooijman, *Proceedings of the Workshop on Physics at HERA*, Volume 1, W. Buchmüller and G. Ingelman (eds.), DESY (1991) p. 23; K. C. Hoeger, *ibid.*, p. 43.
- [30] ZEUS Collab., J. Breitweg et al., *Eur. Phys. J. C* **6**, 43 (1999).
- [31] G.M. Briskin, Ph.D. Thesis, University of Tel Aviv (1998), Report DESY-THESIS-1998-036.
- [32] F. Jacquet and A. Blondel, *Proceedings of the Study for an ep Facility for Europe*, U. Amaldi (Ed.), p. 391, Hamburg, Germany (1979). Also Preprint DESY 79/48.
- [33] P. Capiluppi et al., *Nucl. Phys. B* **70**, 1 (1974);
P. Capiluppi et al., *Nucl. Phys. B* **79**, 189 (1974);
M.G. Albrow et al., *Nucl. Phys. B* **73**, 40 (1974).
- [34] Y. Garcia-Zamora, Ph.D. thesis, University of Geneva (1998) (unpublished).
- [35] ZEUS Collab., J. Breitweg et al., *Eur. Phys. J. C* **2**, 247 (1998).

[36] A. Garfagnini, Ph.D. thesis, University of Calabria (1998) (unpublished).

[37] See e.g.:
 J.A. Crittenden, *Exclusive Production of Neutral Vector Mesons at the Electron-Proton Collider HERA*, Springer Tracts in Modern Physics, Vol. 140, Springer, Berlin, Germany (1997), and references therein;
 H. Abramowicz and A. Caldwell, Rev. Mod. Phys. **71**, 1275 (1999), and references therein.

[38] M.C. Petrucci, Ph.D. thesis, University of Torino (1999), unpublished.

[39] S. Catani et al., Phys. Lett. **B 269**, 432 (1991).

[40] ZEUS Collab., J. Breitweg et al., Z. Phys. **C 75**, 421 (1997).

[41] M. Kasprzak, Ph.D. thesis, University of Warsaw (1996), Internal Report DESY-F35D-96-16.

[42] M. Inuzuka, Ph.D. thesis, University of Tokyo (1999), KEK Report 99-9.

[43] K. Kwiatkowski, H. Spiesberger and H.-J. Möhring, Comp. Phys. Comm. **69**, 155 (1992).

[44] H. Jung, Comp. Phys. Comm. **86**, 147 (1995).

[45] C.-P. Fagerstroem, Ph.D. Thesis, University of Toronto (1999), DESY Report DESY-THESIS-1999-039.

[46] R. Brun et al., *GEANT3*, Technical Report CERN DD/EE/84-1, CERN, 1987.

[47] T. Sjöstrand, Comp. Phys. Comm. **82**, 74 (1994).

[48] G. A. Schüler and H. Spiesberger, *Proceedings of the Workshop on Physics at HERA*, Volume 3, W. Buchmüller and G. Ingelman (eds.), DESY (1991), p. 1419;
 H. Spiesberger, DJANGOH, <http://www.desy.de/~hspiesb/djangoh.html>.

[49] G. Ingelman, A. Edin and J. Rathsman, Comp. Phys. Comm. **101**, 108 (1997).

[50] F.O. Durães, F.S. Navarra and G. Wilk, Phys. Rev. **D 58**, 094034 (1998).

[51] G.N. Fowler et al., Phys. Rev. **C 40**, 1219 (1989).

[52] ZEUS Collab., M. Derrick et al., Z. Phys. **C 68**, 569 (1995).

[53] H. Holtmann et al., Z. Phys. **C 69**, 297 (1996).

[54] J. Whitmore et al., Phys. Rev. **D 11**, 3124 (1975).

[55] S.N. Ganguli and D.P. Roy, Phys. Rep. **67**, 201 (1980).

[56] M. Batista and R.J.M. Covolan, Phys. Rev. **D 59**, 054006 (1999).

[57] F.O. Durães, F.S. Navarra and G. Wilk, hep-ph/0209328 (2002).

- [58] N.N. Nikolaev, private communication.
- [59] ZEUS Collab., J. Breitweg et al., Eur. Phys. J. **C 2**, 237 (1998).
- [60] N.N. Nikolaev, Acta Phys. Pol. **B 29**, 2425 (1998).
- [61] M. Botje, Eur. Phys. J. **C 14**, 285 (2000).

Table 1: *Fraction of events with $\eta_{\max} < 2.5$. Statistical uncertainties are given; systematic uncertainties mostly cancel in the ratio.*

x_L	$N_{\text{LP}}(\eta_{\max} < 2.5)/N_{\text{LP}}$
BPC	
0.63	0.054 ± 0.030
0.66	0.116 ± 0.033
0.69	0.075 ± 0.018
0.72	0.070 ± 0.020
0.75	0.083 ± 0.021
0.78	0.099 ± 0.020
0.81	0.077 ± 0.018
0.84	0.044 ± 0.014
0.87	0.066 ± 0.017
0.90	0.042 ± 0.014
0.93	0.011 ± 0.008
0.96	0.040 ± 0.016
0.99	0.355 ± 0.064
1.00	0.812 ± 0.036
DIS	
0.63	0.0674 ± 0.0093
0.66	0.0567 ± 0.0081
0.69	0.0728 ± 0.0072
0.72	0.0603 ± 0.0063
0.75	0.0543 ± 0.0057
0.78	0.0507 ± 0.0050
0.81	0.0597 ± 0.0047
0.84	0.0495 ± 0.0049
0.87	0.0364 ± 0.0040
0.90	0.0421 ± 0.0047
0.93	0.0304 ± 0.0053
0.96	0.0805 ± 0.0132
0.99	0.3445 ± 0.0231
1.00	0.7683 ± 0.0164

Table 2: The normalised cross-section $(1/\sigma_{\text{tot}}) \cdot d\sigma_{\gamma^* p \rightarrow X p} / dx_L$ for the BPC and DIS data in the region $p_T^2 < 0.5 \text{ GeV}^2$. The two rightmost values indicate the statistical and systematic uncertainties, respectively.

x_L	$(1/\sigma_{\text{tot}}) \cdot d\sigma_{\gamma^* p \rightarrow X p} / dx_L$
BPC	
0.65	$0.339 \pm 0.022 \pm 0.050$
0.75	$0.399 \pm 0.019 \pm 0.048$
0.83	$0.330 \pm 0.014 \pm 0.049$
0.93	$0.331 \pm 0.021 \pm 0.040$
0.99	$3.60 \pm 0.37 \pm 0.54$
DIS	
0.62	$0.413 \pm 0.019 \pm 0.091$
0.65	$0.431 \pm 0.017 \pm 0.065$
0.69	$0.462 \pm 0.016 \pm 0.056$
0.71	$0.445 \pm 0.015 \pm 0.066$
0.75	$0.421 \pm 0.012 \pm 0.088$
0.77	$0.433 \pm 0.012 \pm 0.048$
0.81	$0.379 \pm 0.010 \pm 0.046$
0.83	$0.359 \pm 0.009 \pm 0.029$
0.87	$0.368 \pm 0.010 \pm 0.037$
0.89	$0.333 \pm 0.010 \pm 0.030$
0.93	$0.289 \pm 0.012 \pm 0.026$
0.95	$0.46 \pm 0.03 \pm 0.11$
0.99	$2.48 \pm 0.12 \pm 0.37$

Table 3: The normalised cross-section $(1/\sigma_{\text{tot}}) \cdot d\sigma_{\gamma^* p \rightarrow X p} / dx_L$ for the photoproduction, BPC and DIS data for $p_T^2 < 0.04 \text{ GeV}^2$. The two rightmost values indicate the statistical and systematic uncertainties, respectively.

x_L	$(1/\sigma_{\text{tot}}) \cdot d\sigma_{\gamma^* p \rightarrow X p} / dx_L$
Photoproduction	
0.64	$0.110 \pm 0.017 \pm 0.022$
0.70	$0.081 \pm 0.008 \pm 0.016$
0.76	$0.079 \pm 0.006 \pm 0.012$
0.82	$0.090 \pm 0.006 \pm 0.012$
0.88	$0.080 \pm 0.006 \pm 0.012$
BPC	
0.65	$0.084 \pm 0.007 \pm 0.013$
0.75	$0.099 \pm 0.005 \pm 0.012$
0.83	$0.081 \pm 0.005 \pm 0.012$
0.93	$0.0697 \pm 0.0100 \pm 0.0084$
DIS	
0.62	$0.111 \pm 0.008 \pm 0.024$
0.65	$0.105 \pm 0.006 \pm 0.016$
0.69	$0.110 \pm 0.005 \pm 0.013$
0.71	$0.103 \pm 0.004 \pm 0.015$
0.75	$0.095 \pm 0.003 \pm 0.020$
0.77	$0.102 \pm 0.003 \pm 0.011$
0.81	$0.092 \pm 0.003 \pm 0.011$
0.83	$0.0910 \pm 0.0030 \pm 0.0073$
0.87	$0.0910 \pm 0.0040 \pm 0.0091$
0.89	$0.0820 \pm 0.0050 \pm 0.0075$

Table 4: The slopes, b , from fits of the functional form $e^{-bp_T^2}$ to $d\sigma_{\gamma^* p \rightarrow X p}/dp_T^2$ for leading protons as a function of x_L for the BPC and DIS data samples. The two rightmost values indicate the statistical and systematic uncertainties, respectively.

x_L	b (GeV $^{-2}$)
BPC	
0.65	$7.5 \pm 1.2^{+0.4}_{-1.9}$
0.75	$7.6 \pm 1.0^{+1.2}_{-1.1}$
0.83	$6.2 \pm 1.2^{+1.2}_{-0.7}$
0.93	$4.5 \pm 1.2^{+1.5}_{-0.8}$
DIS	
0.62	$7.4 \pm 1.2^{+1.0}_{-1.3}$
0.65	$7.7 \pm 0.8^{+2.0}_{-1.2}$
0.69	$7.3 \pm 0.6^{+0.8}_{-0.8}$
0.71	$6.8 \pm 0.6^{+0.3}_{-0.6}$
0.75	$6.1 \pm 0.6^{+1.2}_{-1.2}$
0.77	$6.8 \pm 0.7^{+0.4}_{-0.4}$
0.81	$7.9 \pm 0.9^{+0.8}_{-0.9}$
0.83	$7.3 \pm 0.8^{+0.6}_{-0.9}$
0.87	$7.2 \pm 0.7^{+1.1}_{-1.8}$
0.89	$6.6 \pm 0.7^{+0.6}_{-0.5}$
0.93	$5.9 \pm 0.9^{+1.2}_{-1.0}$
0.95	$4.4 \pm 1.7^{+1.5}_{-0.4}$
0.99	$7.0 \pm 0.9^{+1.9}_{-1.1}$

Table 5: The ratio $r^{\text{LP}(3)} = \bar{F}_2^{\text{LP}(3)}/F_2$ as a function of x_L , x and Q^2 (BPC sample), for protons with $p_T^2 < 0.5$ GeV 2 . The two rightmost values indicate the statistical and systematic uncertainties, respectively.

Q^2 (GeV 2)	x	x_L	$r^{\text{LP}(3)}$
0.2	7.4E-06	0.67	$0.310 \pm 0.050 \pm 0.056$
0.2	7.4E-06	0.79	$0.408 \pm 0.042 \pm 0.049$
0.2	7.4E-06	0.91	$0.367 \pm 0.049 \pm 0.037$
0.2	4.9E-06	0.67	$0.308 \pm 0.052 \pm 0.055$
0.2	4.9E-06	0.79	$0.331 \pm 0.039 \pm 0.040$
0.2	4.9E-06	0.91	$0.361 \pm 0.050 \pm 0.036$
0.2	3.5E-06	0.67	$0.281 \pm 0.063 \pm 0.051$
0.2	3.5E-06	0.79	$0.333 \pm 0.049 \pm 0.040$
0.2	3.5E-06	0.91	$0.377 \pm 0.065 \pm 0.038$
0.4	2.6E-05	0.67	$0.357 \pm 0.031 \pm 0.064$
0.4	2.6E-05	0.79	$0.356 \pm 0.022 \pm 0.043$
0.4	2.6E-05	0.91	$0.317 \pm 0.026 \pm 0.032$
0.4	1.3E-05	0.67	$0.356 \pm 0.061 \pm 0.064$
0.4	1.3E-05	0.79	$0.405 \pm 0.047 \pm 0.049$
0.4	1.3E-05	0.91	$0.265 \pm 0.047 \pm 0.027$
0.4	8.8E-06	0.67	$0.357 \pm 0.084 \pm 0.064$
0.4	8.8E-06	0.79	$0.317 \pm 0.057 \pm 0.038$
0.4	8.8E-06	0.91	$0.298 \pm 0.068 \pm 0.030$
0.6	4.3E-05	0.67	$0.438 \pm 0.063 \pm 0.079$
0.6	4.3E-05	0.79	$0.386 \pm 0.043 \pm 0.046$
0.6	4.3E-05	0.91	$0.354 \pm 0.051 \pm 0.035$

Table 6: The ratio $r^{\text{LP}(3)} = \bar{F}_2^{\text{LP}(3)}/F_2$ as a function of x_L , x and Q^2 (DIS sample, up to $Q^2 = 12 \text{ GeV}^2$), for protons with $p_T^2 < 0.5 \text{ GeV}^2$. The two rightmost values indicate the statistical and systematic uncertainties, respectively.

Q^2 (GeV 2)	x	x_L	$r^{\text{LP}(3)}$
4.0	1.5E-04	0.67	$0.344 \pm 0.033 \pm 0.062$
4.0	1.5E-04	0.79	$0.345 \pm 0.023 \pm 0.041$
4.0	1.5E-04	0.91	$0.326 \pm 0.029 \pm 0.033$
4.0	2.5E-04	0.67	$0.327 \pm 0.035 \pm 0.059$
4.0	2.5E-04	0.79	$0.353 \pm 0.026 \pm 0.042$
4.0	2.5E-04	0.91	$0.313 \pm 0.031 \pm 0.031$
4.0	4.4E-04	0.67	$0.367 \pm 0.035 \pm 0.066$
4.0	4.4E-04	0.79	$0.335 \pm 0.024 \pm 0.040$
4.0	4.4E-04	0.91	$0.305 \pm 0.029 \pm 0.030$
4.0	9.8E-04	0.67	$0.443 \pm 0.040 \pm 0.080$
4.0	9.8E-04	0.79	$0.354 \pm 0.026 \pm 0.042$
4.0	9.8E-04	0.91	$0.303 \pm 0.030 \pm 0.030$
8.0	2.5E-04	0.67	$0.398 \pm 0.031 \pm 0.072$
8.0	2.5E-04	0.79	$0.359 \pm 0.021 \pm 0.043$
8.0	2.5E-04	0.91	$0.382 \pm 0.028 \pm 0.038$
8.0	4.4E-04	0.67	$0.387 \pm 0.028 \pm 0.070$
8.0	4.4E-04	0.79	$0.409 \pm 0.020 \pm 0.049$
8.0	4.4E-04	0.91	$0.335 \pm 0.023 \pm 0.033$
8.0	9.8E-04	0.67	$0.451 \pm 0.031 \pm 0.081$
8.0	9.8E-04	0.79	$0.420 \pm 0.021 \pm 0.050$
8.0	9.8E-04	0.91	$0.375 \pm 0.026 \pm 0.038$
8.0	2.2E-03	0.67	$0.515 \pm 0.050 \pm 0.093$
8.0	2.2E-03	0.79	$0.380 \pm 0.031 \pm 0.046$
8.0	2.2E-03	0.91	$0.421 \pm 0.041 \pm 0.042$
12.0	4.4E-04	0.67	$0.355 \pm 0.029 \pm 0.064$
12.0	4.4E-04	0.79	$0.379 \pm 0.022 \pm 0.046$
12.0	4.4E-04	0.91	$0.396 \pm 0.028 \pm 0.040$
12.0	9.8E-04	0.67	$0.416 \pm 0.029 \pm 0.075$
12.0	9.8E-04	0.79	$0.387 \pm 0.020 \pm 0.046$
12.0	9.8E-04	0.91	$0.369 \pm 0.025 \pm 0.037$
12.0	2.2E-03	0.67	$0.437 \pm 0.039 \pm 0.079$
12.0	2.2E-03	0.79	$0.407 \pm 0.027 \pm 0.049$
12.0	2.2E-03	0.91	$0.445 \pm 0.036 \pm 0.044$
12.0	4.0E-03	0.67	$0.462 \pm 0.067 \pm 0.083$
12.0	4.0E-03	0.79	$0.427 \pm 0.046 \pm 0.051$
12.0	4.0E-03	0.91	$0.349 \pm 0.053 \pm 0.035$

Table 7: The ratio $r^{\text{LP}(3)} = \bar{F}_2^{\text{LP}(3)}/F_2$ as a function of x_L , x and Q^2 (DIS sample, for $Q^2 > 12 \text{ GeV}^2$), for protons with $p_T^2 < 0.5 \text{ GeV}^2$. The two rightmost values indicate the statistical and systematic uncertainties, respectively.

Q^2 (GeV 2)	x	x_L	$r^{\text{LP}(3)}$
21.0	9.8E-04	0.67	$0.423 \pm 0.027 \pm 0.076$
21.0	9.8E-04	0.79	$0.387 \pm 0.019 \pm 0.046$
21.0	9.8E-04	0.91	$0.360 \pm 0.023 \pm 0.036$
21.0	2.2E-03	0.67	$0.437 \pm 0.034 \pm 0.079$
21.0	2.2E-03	0.79	$0.427 \pm 0.024 \pm 0.051$
21.0	2.2E-03	0.91	$0.379 \pm 0.029 \pm 0.038$
21.0	4.0E-03	0.67	$0.486 \pm 0.049 \pm 0.087$
21.0	4.0E-03	0.79	$0.390 \pm 0.031 \pm 0.047$
21.0	4.0E-03	0.91	$0.361 \pm 0.038 \pm 0.036$
21.0	5.9E-03	0.67	$0.474 \pm 0.066 \pm 0.085$
21.0	5.9E-03	0.79	$0.372 \pm 0.042 \pm 0.045$
21.0	5.9E-03	0.91	$0.466 \pm 0.059 \pm 0.047$
46.0	2.2E-03	0.67	$0.452 \pm 0.043 \pm 0.081$
46.0	2.2E-03	0.79	$0.372 \pm 0.028 \pm 0.045$
46.0	2.2E-03	0.91	$0.490 \pm 0.040 \pm 0.049$
46.0	4.0E-03	0.67	$0.444 \pm 0.055 \pm 0.080$
46.0	4.0E-03	0.79	$0.433 \pm 0.039 \pm 0.052$
46.0	4.0E-03	0.91	$0.360 \pm 0.045 \pm 0.036$
46.0	5.9E-03	0.67	$0.435 \pm 0.064 \pm 0.078$
46.0	5.9E-03	0.79	$0.348 \pm 0.041 \pm 0.042$
46.0	5.9E-03	0.91	$0.436 \pm 0.059 \pm 0.044$
46.0	1.0E-02	0.67	$0.453 \pm 0.050 \pm 0.081$
46.0	1.0E-02	0.79	$0.412 \pm 0.034 \pm 0.049$
46.0	1.0E-02	0.91	$0.409 \pm 0.043 \pm 0.041$
130.0	5.9E-03	0.67	$0.441 \pm 0.094 \pm 0.079$
130.0	5.9E-03	0.79	$0.327 \pm 0.058 \pm 0.039$
130.0	5.9E-03	0.91	$0.528 \pm 0.094 \pm 0.053$
130.0	1.0E-02	0.67	$0.408 \pm 0.060 \pm 0.073$
130.0	1.0E-02	0.79	$0.505 \pm 0.048 \pm 0.061$
130.0	1.0E-02	0.91	$0.358 \pm 0.051 \pm 0.036$
130.0	2.5E-02	0.67	$0.421 \pm 0.069 \pm 0.076$
130.0	2.5E-02	0.79	$0.430 \pm 0.050 \pm 0.052$
130.0	2.5E-02	0.91	$0.403 \pm 0.062 \pm 0.040$

Table 8: The ratio $r^{\text{LP}(2)} = \bar{F}_2^{\text{LP}(2)}/F_2$ as a function of x for fixed Q^2 values, for protons with $0.6 < x_L < 0.97$ and $p_T^2 < 0.5 \text{ GeV}^2$. The statistical uncertainty is given. A fully correlated systematic uncertainty of $\pm 13\%$ is not included.

Q^2 (GeV 2)	x	$r^{\text{LP}(2)}$
0.20	3.5E-06	0.118 ± 0.012
0.20	4.9E-06	0.1177 ± 0.0093
0.20	7.4E-06	0.1309 ± 0.0095
0.36	8.8E-06	0.113 ± 0.014
0.36	1.3E-05	0.124 ± 0.010
0.36	2.6E-05	0.1211 ± 0.0092
0.60	4.3E-05	0.137 ± 0.010
4.0	9.8E-04	0.1281 ± 0.0063
4.0	4.4E-04	0.1186 ± 0.0058
4.0	2.5E-04	0.1190 ± 0.0062
4.0	1.5E-04	0.1206 ± 0.0056
8.0	2.2E-03	0.1507 ± 0.0079
8.0	9.8E-04	0.1473 ± 0.0052
8.0	4.4E-04	0.1358 ± 0.0048
8.0	2.5E-04	0.1332 ± 0.0053
12.0	4.0E-03	0.147 ± 0.011
12.0	2.2E-03	0.1511 ± 0.0067
12.0	9.8E-04	0.1382 ± 0.0049
12.0	4.4E-04	0.1345 ± 0.0053
21.0	5.9E-03	0.151 ± 0.011
21.0	4.0E-03	0.1438 ± 0.0077
21.0	2.2E-03	0.1477 ± 0.0058
21.0	9.8E-04	0.1377 ± 0.0046
46.0	1.0E-02	0.1496 ± 0.0084
46.0	5.9E-03	0.140 ± 0.011
46.0	4.0E-03	0.1472 ± 0.0092
46.0	2.2E-03	0.1512 ± 0.0072
130.0	2.5E-02	0.149 ± 0.012
130.0	1.0E-02	0.156 ± 0.011
130.0	5.9E-03	0.147 ± 0.016

Table 9: The average ratio $\langle r^{\text{LP}(2)} \rangle = \bar{F}_2^{\text{LP}(2)} / F_2$ as a function of Q^2 for $0.6 < x_L < 0.97$ and $p_T^2 < 0.5 \text{ GeV}^2$. The statistical uncertainty is given. A fully correlated systematic uncertainty of 13% is not included.

Q^2 (GeV 2)	$\langle r^{\text{LP}(2)} \rangle$
0.29	0.1230 ± 0.0033
5.21	0.1312 ± 0.0020
16.60	0.1397 ± 0.0021
69.00	0.1471 ± 0.0036

Table 10: The average ratio $\langle r^{\text{LP}(2)} \rangle$ as a function of Q^2 for two different p_T^2 ranges normalised to the value at $Q^2 = 0.25 \text{ GeV}^2$. The statistical uncertainty is given; systematic errors mostly cancel in the ratio.

Q^2 (GeV 2)	$\langle r^{\text{LP}(2)}(Q^2) \rangle / \langle r^{\text{LP}(2)}(Q^2 = 0.25 \text{ GeV}^2) \rangle$	
	$p_T^2 < 0.04 \text{ GeV}^2$	$p_T^2 < 0.5 \text{ GeV}^2$
0.002	0.941 ± 0.033	
0.29	1.000 ± 0.000	1.000 ± 0.000
5.21	1.062 ± 0.022	1.067 ± 0.031
16.60	1.115 ± 0.023	1.136 ± 0.031
69.00	1.152 ± 0.039	1.196 ± 0.037

Table 11: *The structure-function $\bar{F}_2^{\text{LP}(2)}$ as a function of x for $0.6 < x_L < 0.97$ and $p_T^2 < 0.5 \text{ GeV}^2$. The statistical uncertainty is given. A fully correlated systematic uncertainty of $\pm 13\%$ is not included, nor is the uncertainty of the F_2 parametrisations used.*

x	Q^2 (GeV 2)	$\bar{F}_2^{\text{LP}(2)}$
3.5E-06	0.2	0.0286 ± 0.0029
4.9E-06	0.2	0.0277 ± 0.0022
7.4E-06	0.2	0.0296 ± 0.0021
8.8E-06	0.4	0.0391 ± 0.0048
1.3E-05	0.4	0.0412 ± 0.0035
2.6E-05	0.4	0.0378 ± 0.0029
4.3E-05	0.6	0.0559 ± 0.0042
1.5E-04	4.0	0.1126 ± 0.0052
2.5E-04	4.0	0.0991 ± 0.0052
4.4E-04	4.0	0.0872 ± 0.0043
9.8E-04	4.0	0.0793 ± 0.0039
2.5E-04	8.0	0.1518 ± 0.0060
4.4E-04	8.0	0.1347 ± 0.0048
9.8E-04	8.0	0.1201 ± 0.0042
2.2E-03	8.0	0.1014 ± 0.0053
4.4E-04	12.0	0.1563 ± 0.0062
9.8E-04	12.0	0.1303 ± 0.0046
2.2E-03	12.0	0.1157 ± 0.0051
4.0E-03	12.0	0.0969 ± 0.0073
9.8E-04	21.0	0.1552 ± 0.0052
2.2E-03	21.0	0.1325 ± 0.0052
4.0E-03	21.0	0.1093 ± 0.0059
5.9E-03	21.0	0.1029 ± 0.0074
2.2E-03	46.0	0.1659 ± 0.0079
4.0E-03	46.0	0.1339 ± 0.0084
5.9E-03	46.0	0.1127 ± 0.0086
1.0E-02	46.0	0.1026 ± 0.0058
5.9E-03	130.0	0.140 ± 0.015
1.0E-02	130.0	0.1240 ± 0.0086
2.5E-02	130.0	0.0880 ± 0.0071

Table 12: The structure function $F_2^{\text{LP}(3)}$ as a function of x_L in bins of x and Q^2 (DIS sample), for protons in a restricted p_T^2 range, $p_T^2 < 0.04 \text{ GeV}^2$. The two rightmost values indicate the statistical and systematic uncertainties, respectively.

Q^2 (GeV 2)	x	x_L	$\bar{F}_2^{\text{LP}(3)}$
4.4	3.3E-04	0.73	$0.0675 \pm 0.0080 \pm 0.0157$
4.4	3.3E-04	0.78	$0.0724 \pm 0.0078 \pm 0.0116$
4.4	3.3E-04	0.83	$0.0756 \pm 0.0082 \pm 0.0106$
4.4	3.3E-04	0.88	$0.0585 \pm 0.0082 \pm 0.0098$
4.4	1.0E-03	0.73	$0.0489 \pm 0.0077 \pm 0.0125$
4.4	1.0E-03	0.78	$0.0552 \pm 0.0077 \pm 0.0101$
4.4	1.0E-03	0.83	$0.0605 \pm 0.0083 \pm 0.0099$
4.4	1.0E-03	0.88	$0.0460 \pm 0.0083 \pm 0.0093$
7.5	3.3E-04	0.73	$0.0962 \pm 0.0079 \pm 0.0209$
7.5	3.3E-04	0.78	$0.0955 \pm 0.0074 \pm 0.0136$
7.5	3.3E-04	0.83	$0.0822 \pm 0.0070 \pm 0.0101$
7.5	3.3E-04	0.88	$0.0855 \pm 0.0083 \pm 0.0115$
7.5	1.0E-03	0.73	$0.0899 \pm 0.0085 \pm 0.0200$
7.5	1.0E-03	0.78	$0.0737 \pm 0.0072 \pm 0.0114$
7.5	1.0E-03	0.83	$0.0682 \pm 0.0071 \pm 0.0094$
7.5	1.0E-03	0.88	$0.0715 \pm 0.0084 \pm 0.0107$
7.5	3.3E-03	0.73	$0.0587 \pm 0.0081 \pm 0.0143$
7.5	3.3E-03	0.78	$0.0563 \pm 0.0075 \pm 0.0100$
7.5	3.3E-03	0.83	$0.0505 \pm 0.0072 \pm 0.0085$
7.5	3.3E-03	0.88	$0.0619 \pm 0.0093 \pm 0.0109$
13.3	1.0E-03	0.73	$0.0957 \pm 0.0078 \pm 0.0208$
13.3	1.0E-03	0.78	$0.1023 \pm 0.0076 \pm 0.0144$
13.3	1.0E-03	0.83	$0.0886 \pm 0.0072 \pm 0.0107$
13.3	1.0E-03	0.88	$0.0729 \pm 0.0074 \pm 0.0101$
13.3	3.3E-03	0.73	$0.0666 \pm 0.0061 \pm 0.0147$
13.3	3.3E-03	0.78	$0.0698 \pm 0.0059 \pm 0.0102$
13.3	3.3E-03	0.83	$0.0677 \pm 0.0059 \pm 0.0084$
13.3	3.3E-03	0.88	$0.0658 \pm 0.0067 \pm 0.0091$
28.6	1.0E-03	0.73	$0.1249 \pm 0.0125 \pm 0.0281$
28.6	1.0E-03	0.78	$0.1290 \pm 0.0119 \pm 0.0195$
28.6	1.0E-03	0.83	$0.1007 \pm 0.0107 \pm 0.0140$
28.6	1.0E-03	0.88	$0.0956 \pm 0.0121 \pm 0.0150$
28.6	3.3E-03	0.73	$0.0906 \pm 0.0089 \pm 0.0203$
28.6	3.3E-03	0.78	$0.0934 \pm 0.0085 \pm 0.0140$
28.6	3.3E-03	0.83	$0.0701 \pm 0.0075 \pm 0.0097$
28.6	3.3E-03	0.88	$0.0758 \pm 0.0089 \pm 0.0114$

Table 13: *Fraction of leading-proton DIS events with exactly two jets with $E_T > 4$ GeV, $r_{\text{LP}}^{\text{jet}}$, as a function of x_L for $p_T^2 < 0.5$ GeV 2 . The two rightmost values indicate the statistical and systematic uncertainties, respectively. The systematic uncertainties are highly correlated.*

x_L	$r_{\text{LP}}^{\text{jet}}$
0.645	$0.0209 \pm 0.0031 \pm 0.0053$
0.735	$0.0254 \pm 0.0023 \pm 0.0062$
0.825	$0.0242 \pm 0.0019 \pm 0.0060$
0.920	$0.0196 \pm 0.0026 \pm 0.0050$

Table 14: *Fraction of leading-proton DIS events with exactly two jets with $E_T > 4$ GeV, $r_{\text{LP}}^{\text{jet}}$, as a function of p_T^2 for $0.6 < x_L < 0.97$. The two rightmost values indicate the statistical and systematic uncertainties, respectively. The systematic uncertainties are highly correlated.*

p_T^2 (GeV 2)	$r_{\text{LP}}^{\text{jet}}$
0.0105	$0.0201 \pm 0.0020 \pm 0.0037$
0.0355	$0.0204 \pm 0.0022 \pm 0.0064$
0.0900	$0.0259 \pm 0.0024 \pm 0.0057$
0.3150	$0.0350 \pm 0.0032 \pm 0.0083$

Table 15: *Ratio of the yield of DIS events with exactly two jets with $E_T > 4$ GeV and an LPS proton to the yield of DIS events with exactly two jets, also with $E_T > 4$ GeV, $r_{\text{jet}}^{\text{LP}}$, as a function of E_T of the higher-energy jet. The statistical uncertainty is given. A fully correlated systematic uncertainty of $\pm 13\%$ is not included.*

E_T (GeV)	$r_{\text{jet}}^{\text{LP}}$
4.8	0.126 ± 0.018
5.8	0.122 ± 0.017
6.8	0.130 ± 0.019
8.0	0.124 ± 0.018
12.3	0.088 ± 0.014

Table 16: *Ratio of the yield of DIS events with exactly two jets with $E_T > 4$ GeV and an LPS proton to the yield of DIS events with exactly two jets, also with $E_T > 4$ GeV, $r_{\text{jet}}^{\text{LP}}$, as a function of Q^2 . The statistical uncertainty is given. A fully correlated systematic uncertainty of $\pm 13\%$ is not included.*

Q^2 (GeV 2)	$r_{\text{jet}}^{\text{LP}}$
6.6	0.123 ± 0.013
19.4	0.097 ± 0.017
36.0	0.111 ± 0.017
106.8	0.121 ± 0.015

Table 17: *Ratio of the yield of DIS events with exactly two jets with $E_T > 4$ GeV and an LPS proton to the yield of DIS events with exactly two jets, also with $E_T > 4$ GeV, $r_{\text{jet}}^{\text{LP}}$, as a function of x . The statistical uncertainty is given. A fully correlated systematic uncertainty of $\pm 13\%$ is not included.*

x	$r_{\text{jet}}^{\text{LP}}$
0.00027	0.131 ± 0.014
0.00093	0.109 ± 0.015
0.0022	0.107 ± 0.015
0.0079	0.109 ± 0.017

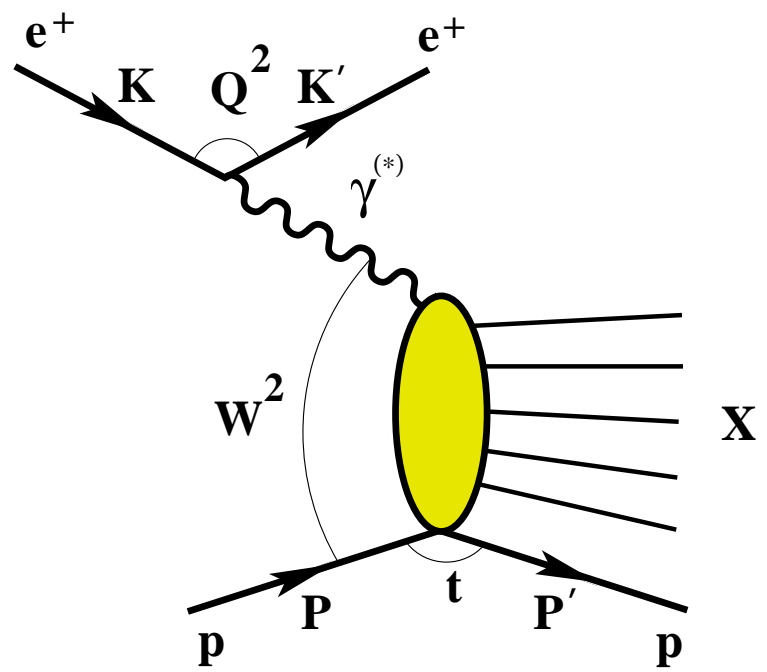


Figure 1: Schematic diagram of the reaction $e^+p \rightarrow e^+Xp$.

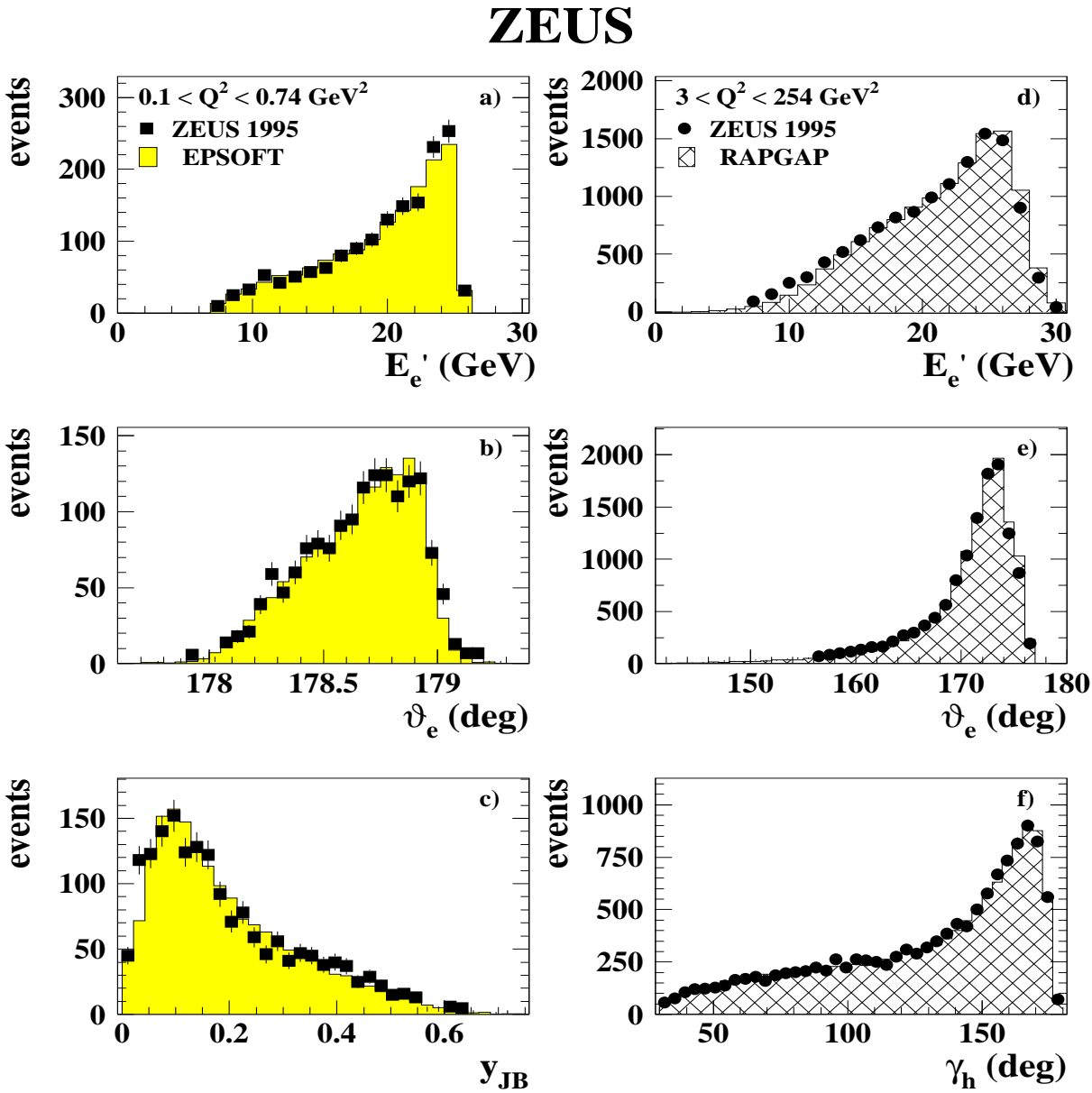


Figure 2: Distributions of the variables a) E'_e , b) ϑ_e and c) y_{JB} for the reconstructed BPC data (squares) and the simulated events (EPSOFT), shown as the shaded histograms (normalised to the data); d) E'_e , e) ϑ_e and f) γ_h for the reconstructed DIS data (dots) and the simulated events (RAPGAP), shown as the hatched histograms (normalised to the data).

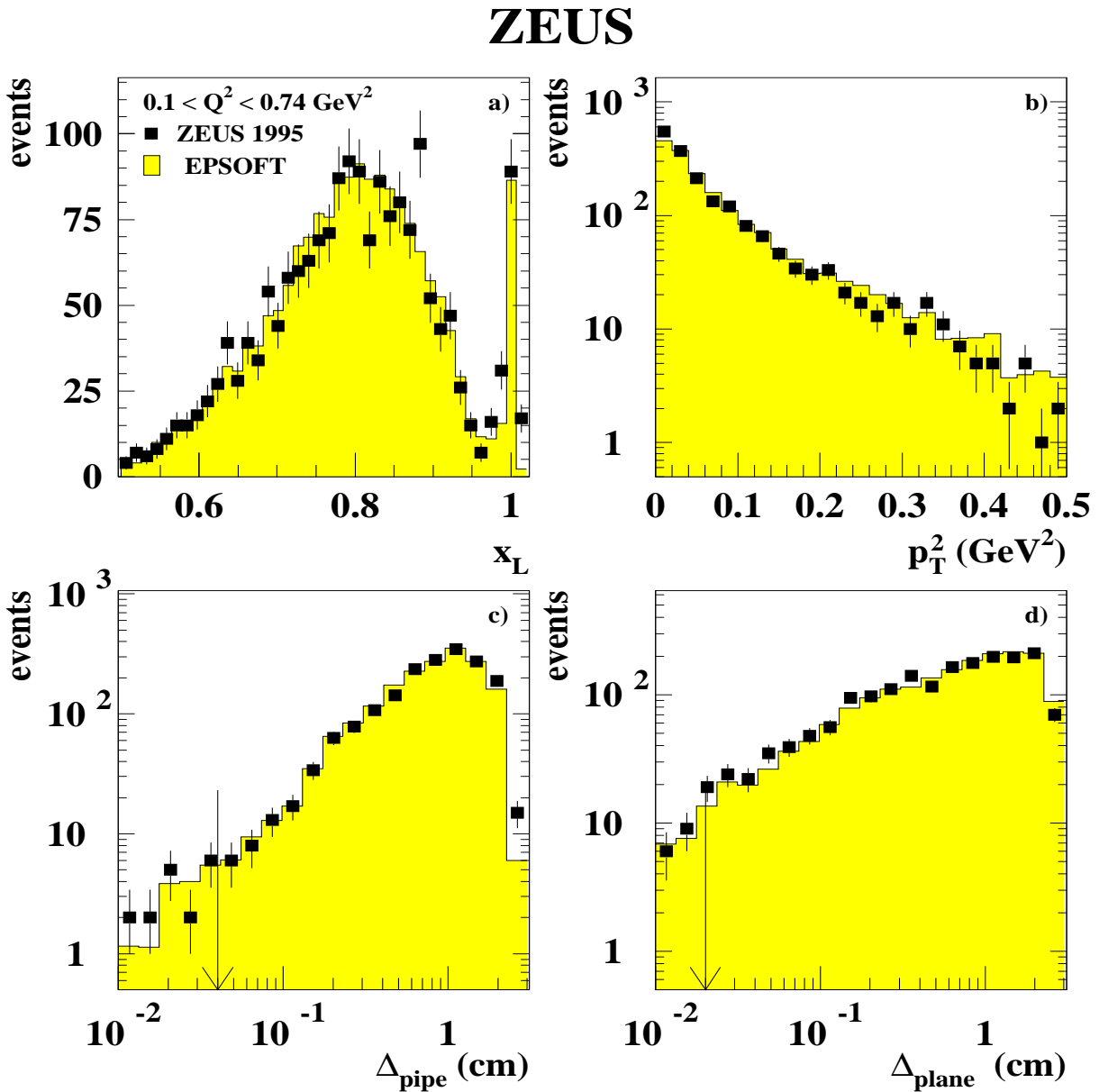


Figure 3: *Distributions of the variables a) x_L , b) p_T^2 , c) Δ_{pipe} and d) Δ_{plane} , for the reconstructed BPC data (squares) and for the simulated events (EPSOFT) shown as the shaded histogram (normalised to the data). The arrows indicate the minimum allowed values of Δ_{pipe} and Δ_{plane} (see text).*

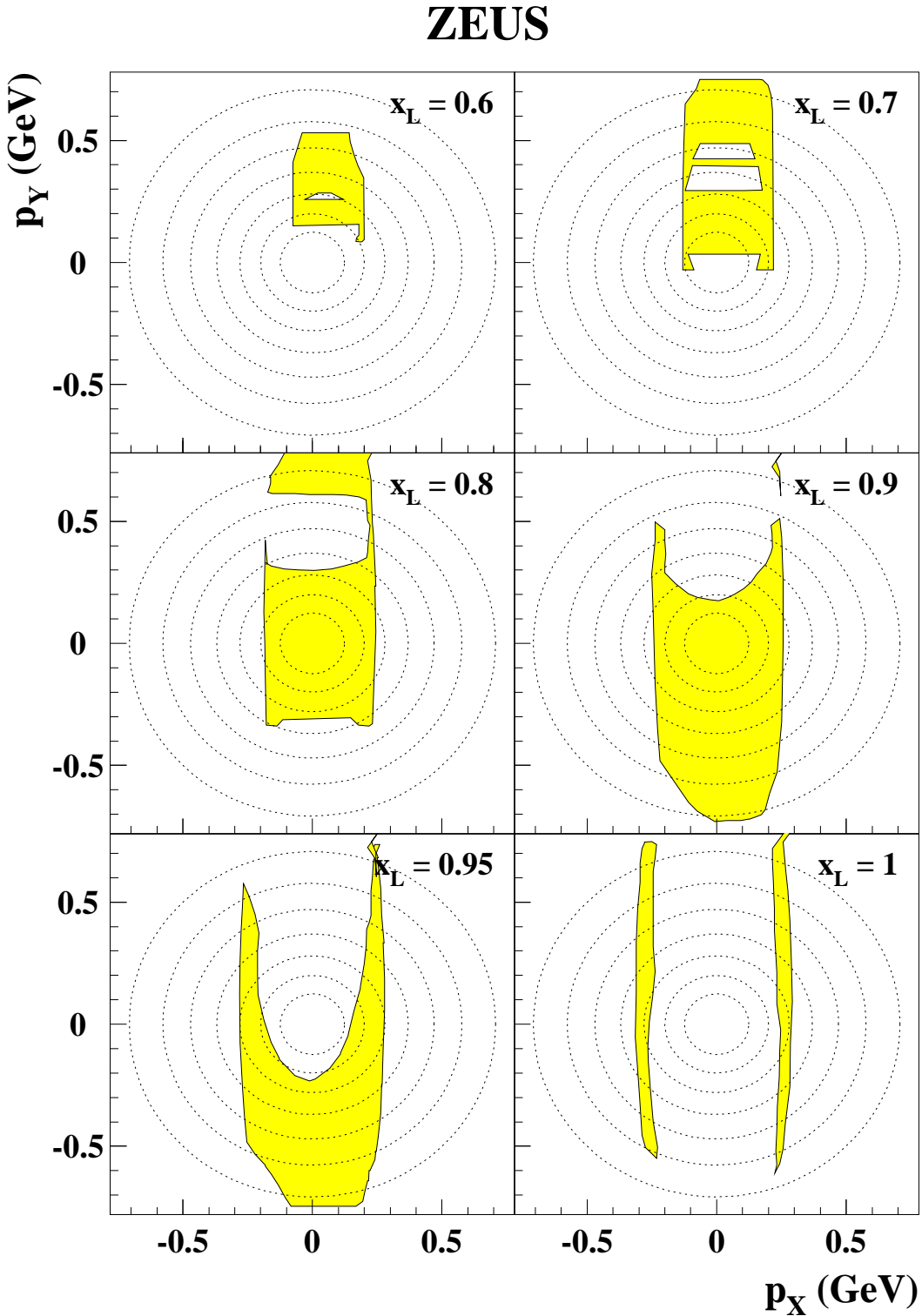


Figure 4: LPS geometrical acceptance for different x_L values as a function of p_x and p_y . The shaded areas indicate the regions of acceptance. The dashed circles indicate the limits of the p_T bins used in the analysis (the bin edges are 0.124 GeV, 0.199 GeV, 0.280 GeV, 0.370 GeV, 0.470 GeV, 0.507 GeV, 0.707 GeV).

ZEUS

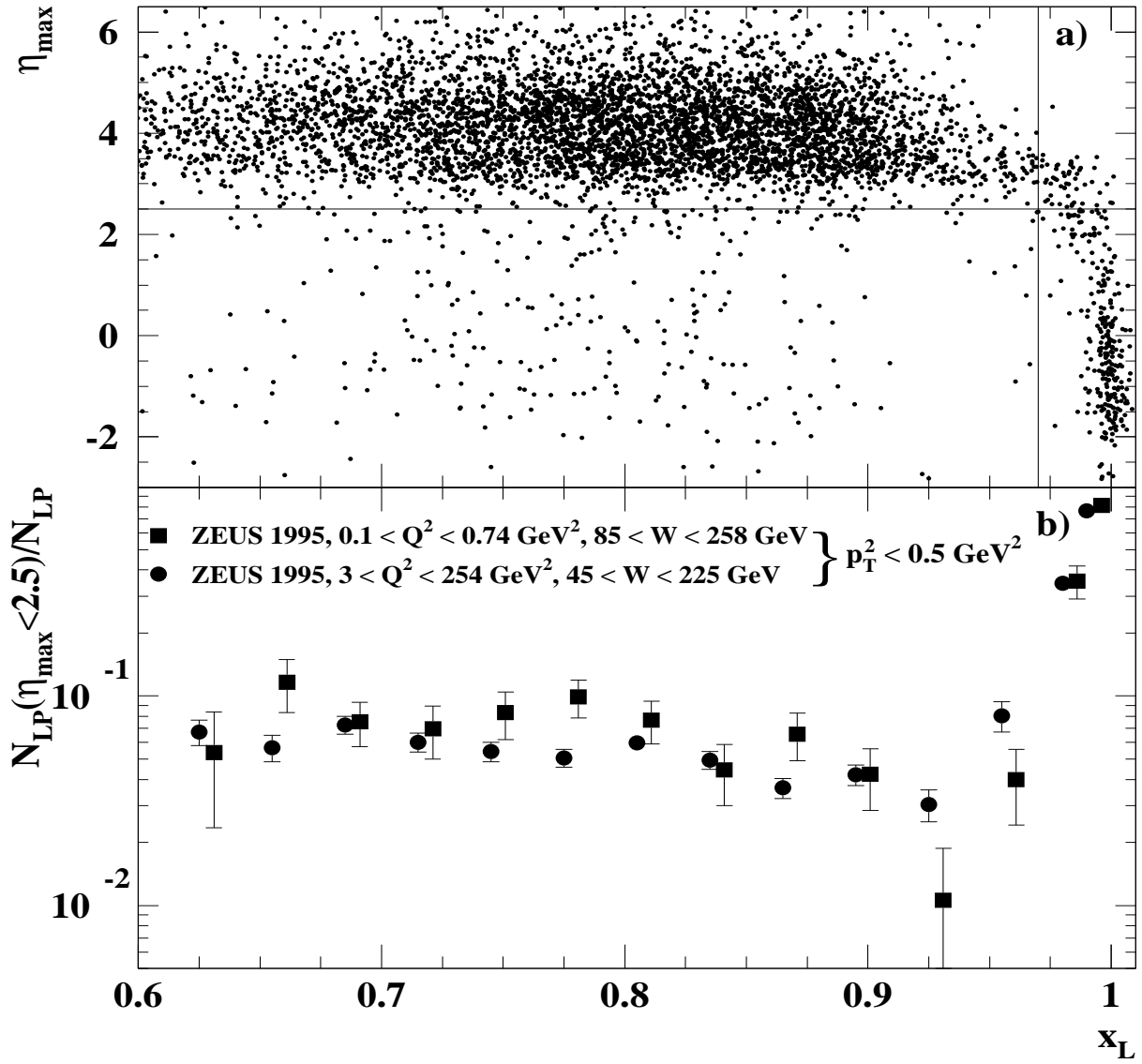


Figure 5: a) Distribution of the DIS events in the (η_{\max}, x_L) plane. The horizontal and vertical lines indicate $\eta_{\max} = 2.5$ and $x_L = 0.97$, respectively. b) Fraction of events with $\eta_{\max} < 2.5$ for both the BPC and the DIS samples. The BPC data are slightly shifted in x_L for clarity of presentation. The bars indicate the statistical uncertainties; systematic uncertainties mostly cancel in the ratio.

ZEUS

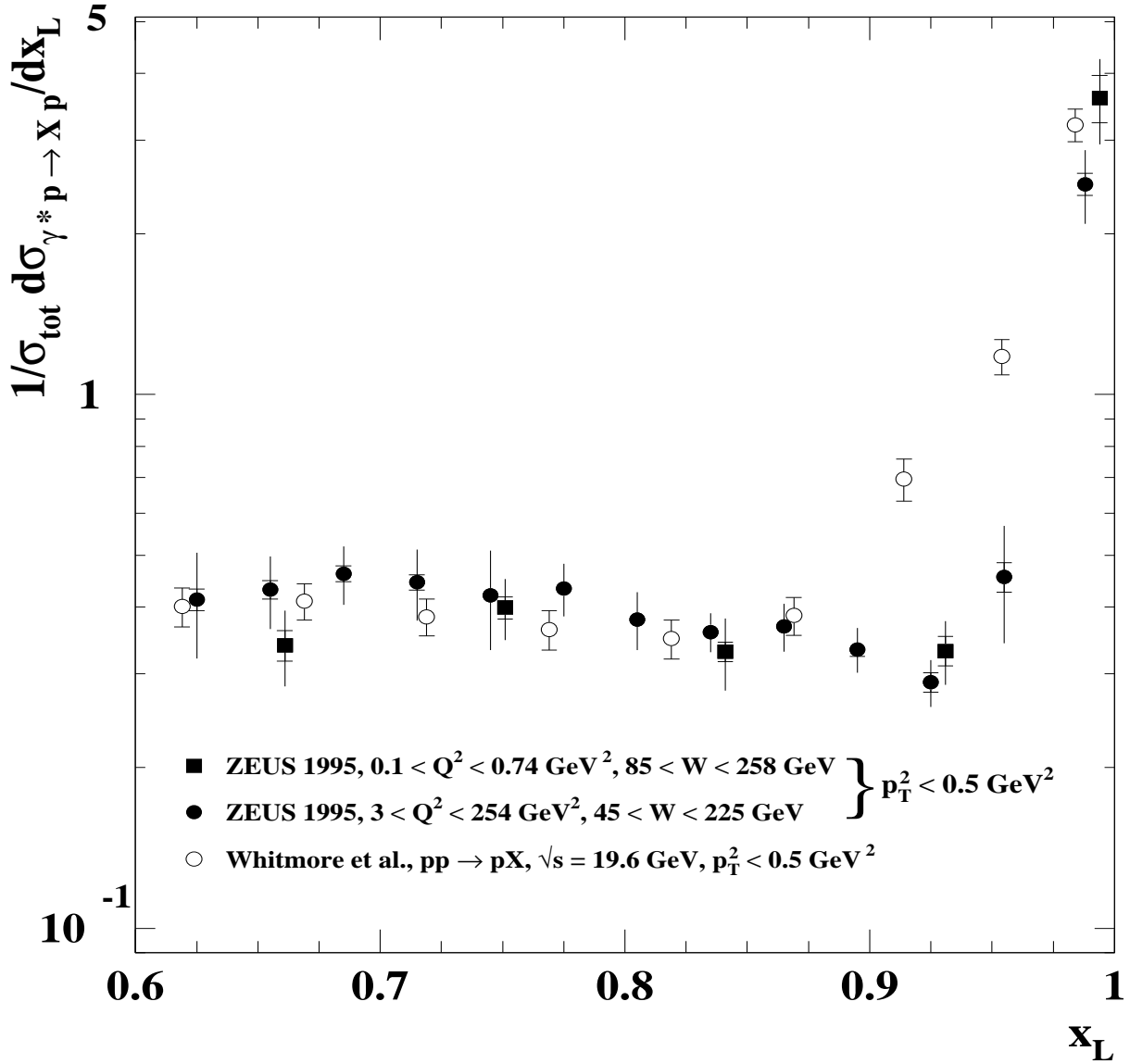


Figure 6: The normalised cross-section $(1/\sigma_{\text{tot}}) \cdot d\sigma_{\gamma^* p \rightarrow Xp} / dx_L$ for the BPC and DIS data compared to the pp data [54] in the region $p_T^2 < 0.5 \text{ GeV}^2$. The inner bars indicate the statistical uncertainties and the outer bars are the statistical and systematic uncertainties summed in quadrature.

ZEUS

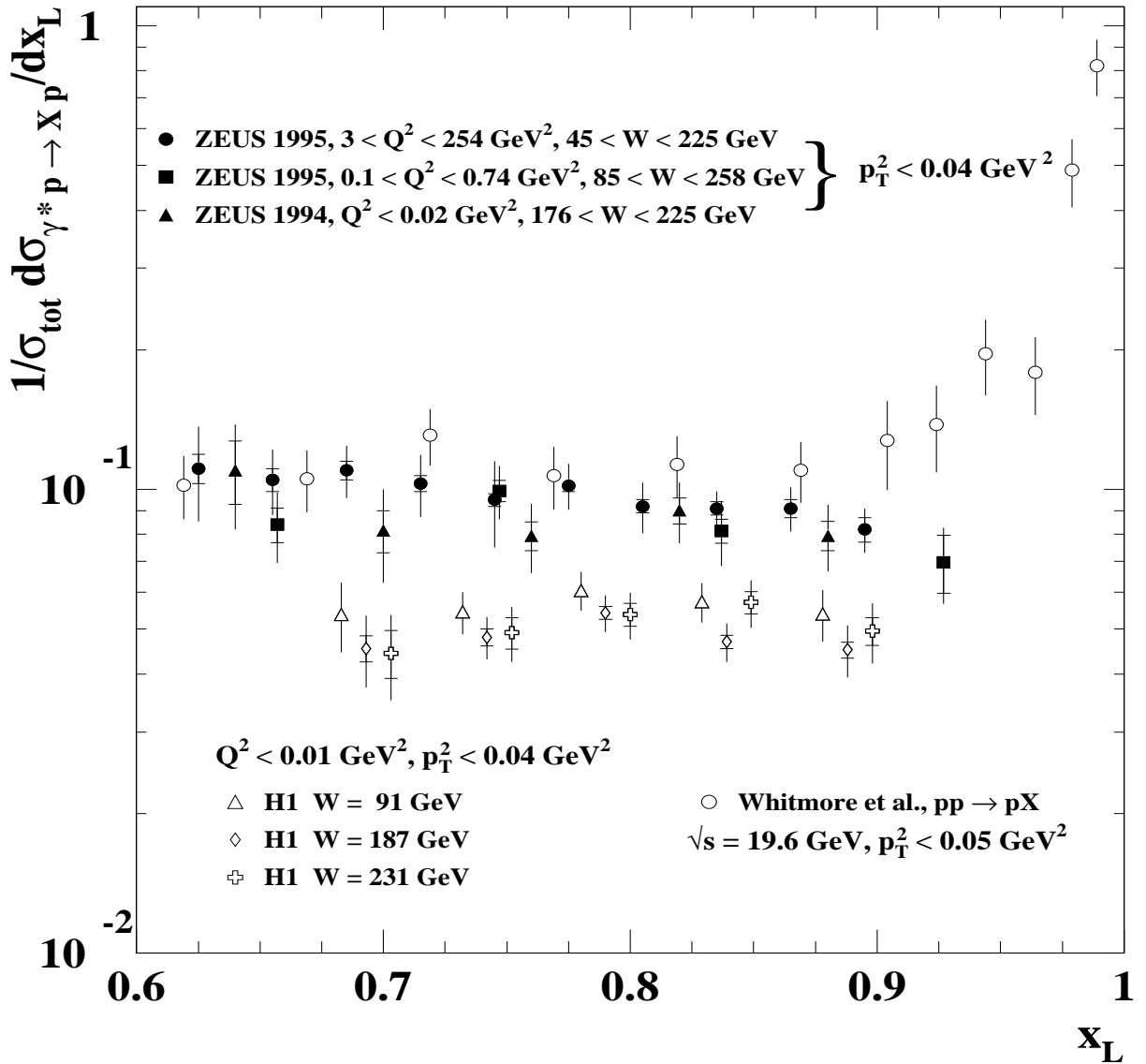


Figure 7: The normalized cross-section $(1/\sigma_{\text{tot}}) \cdot d\sigma_{\gamma^* p \rightarrow Xp} / dx_L$ for the photoproduction, BPC and DIS data compared to the pp data [54] in the region $p_T^2 < 0.04 \text{ GeV}^2$. The inner bars indicate the statistical uncertainties and the outer bars are the statistical and systematic uncertainties summed in quadrature. The H1 results [7] are also shown.

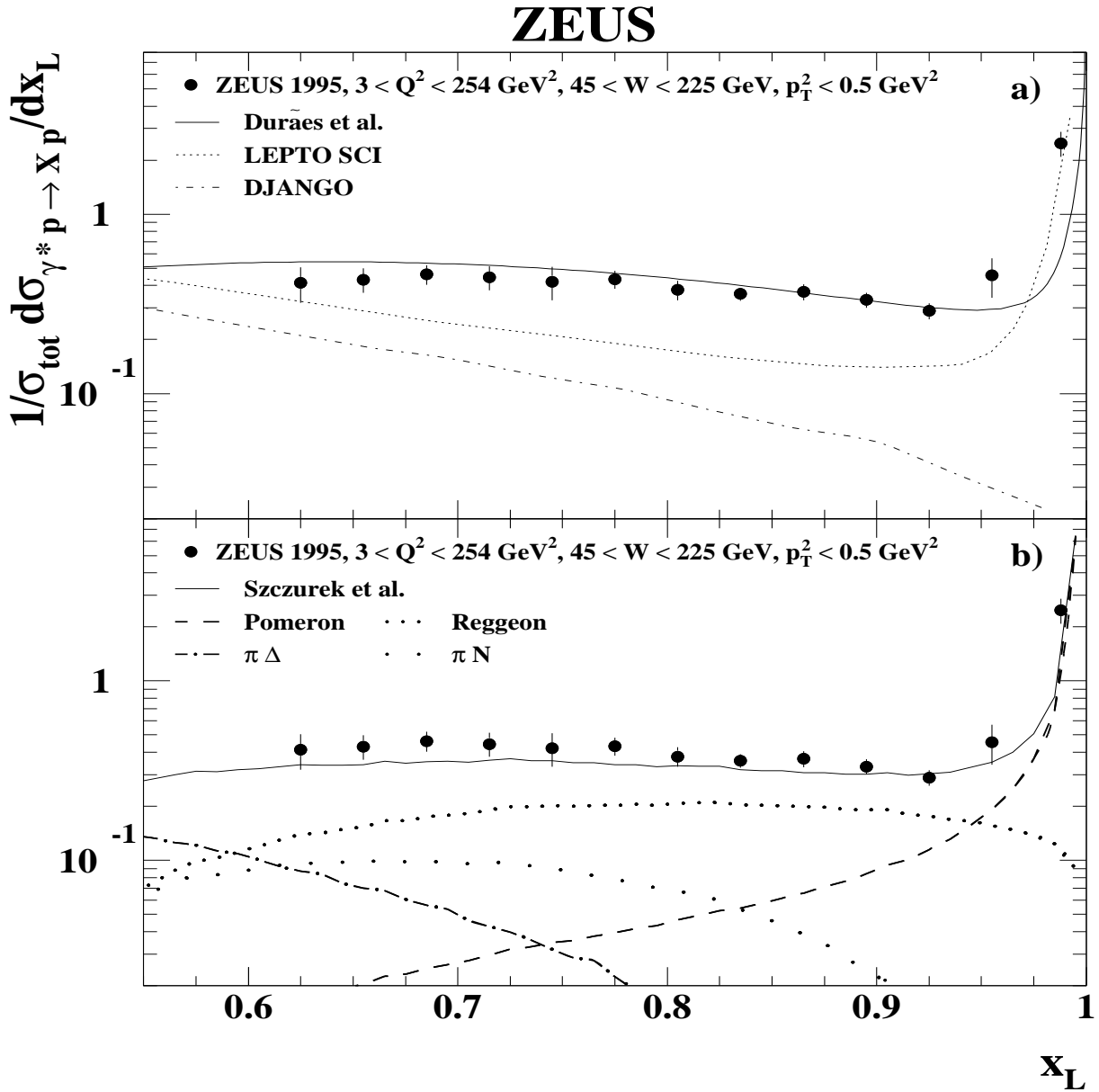


Figure 8: The normalised cross-section $(1/\sigma_{\text{tot}}) \cdot d\sigma_{\gamma^* p \rightarrow Xp} / dx_L$ for the DIS data (as shown in Fig. 6) compared to a) the model of Durães et al. (solid curve), LEPTO6.5 (dashed curve) and DJANGO (dot-dashed curve), and b) to the model of Szczurek et al. (solid curve). For the latter, the individual contributions of Pomeron, Reggeon and pion exchanges are indicated; for pion exchange, the contribution of final states with isospin $I = 1/2$ and $I = 3/2$ are shown separately.

ZEUS

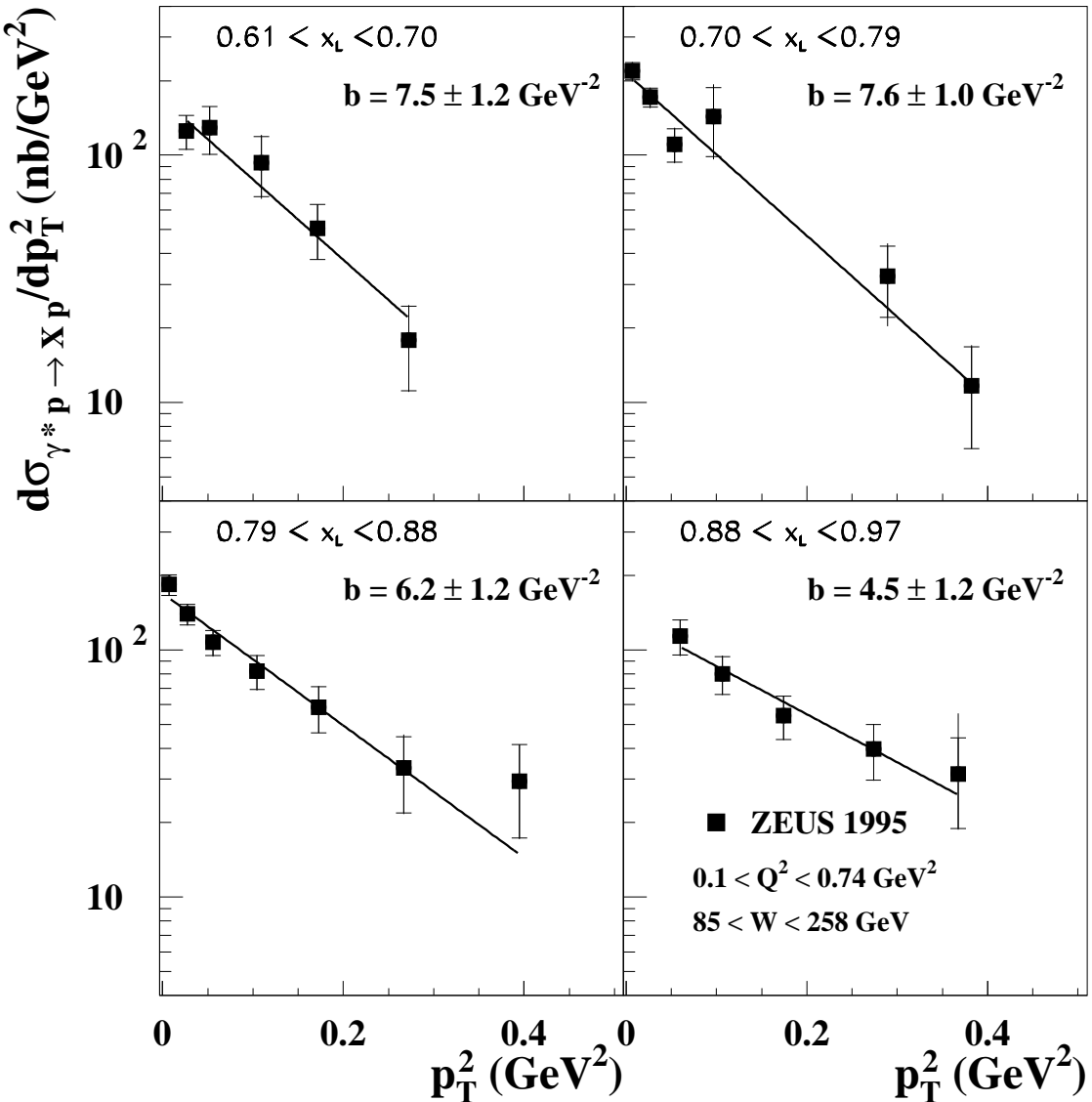


Figure 9: The differential cross-section $d\sigma_{\gamma^* p \rightarrow Xp} / dp_T^2$ for several x_L bins for the BPC sample. The lines represent the results of fits to the functional form $d\sigma_{\gamma^* p \rightarrow Xp} / dp_T^2 \propto e^{-bp_T^2}$. The fitted values of b and their statistical uncertainties are also given. The inner bars indicate the size of the statistical uncertainties, the outer bars show the statistical and systematic uncertainties summed in quadrature.

ZEUS

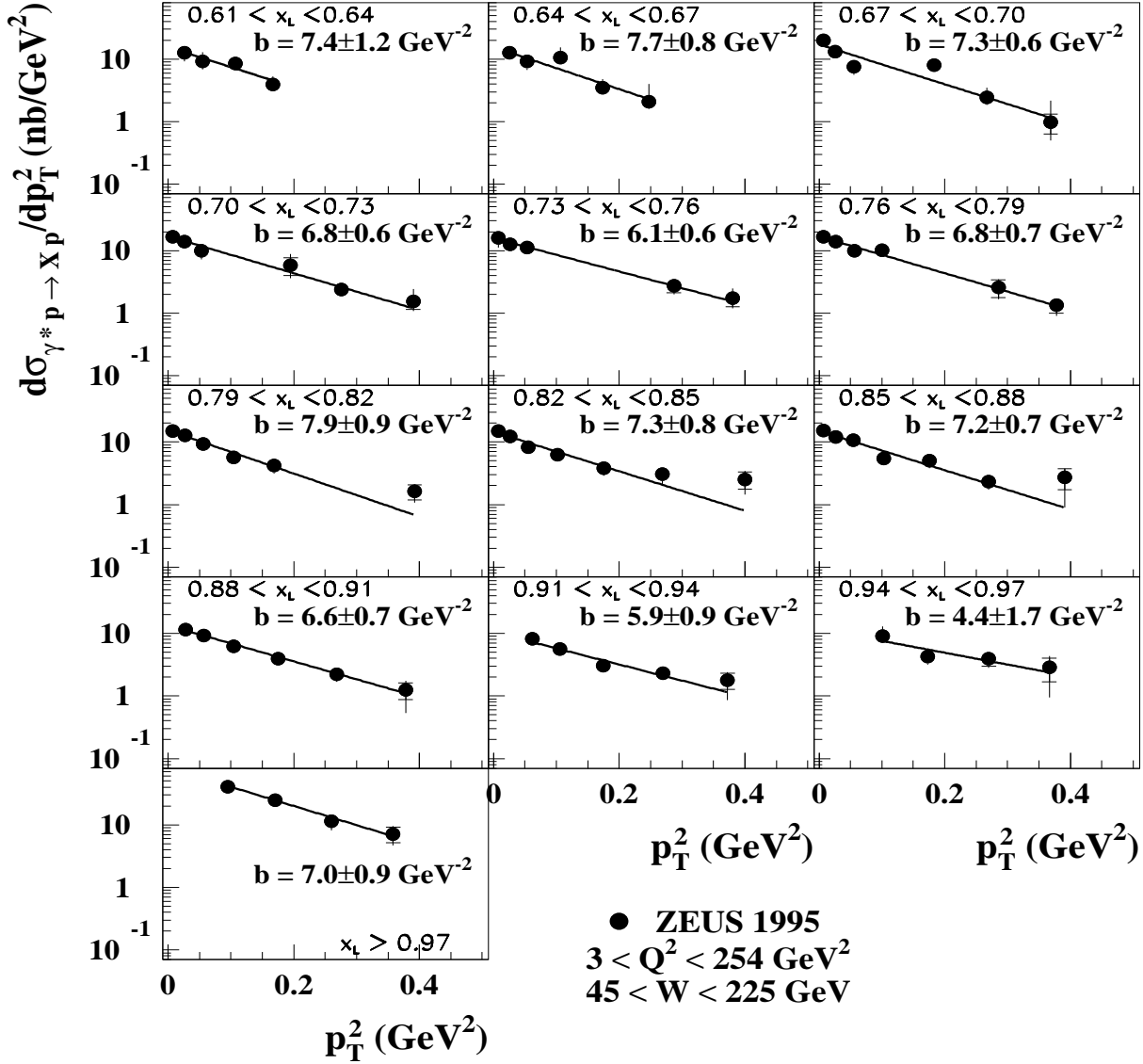


Figure 10: The differential cross-section $d\sigma_{\gamma^* p \rightarrow Xp} / dp_T^2$ for several x_L bins for the DIS sample. The lines represent the results of fits to the functional form $d\sigma_{\gamma^* p \rightarrow Xp} / dp_T^2 \propto e^{-bp_T^2}$. The fitted values of b and their statistical uncertainties are also given. The inner bars indicate the size of the statistical uncertainties, the outer bars show the statistical and systematic uncertainties summed in quadrature.

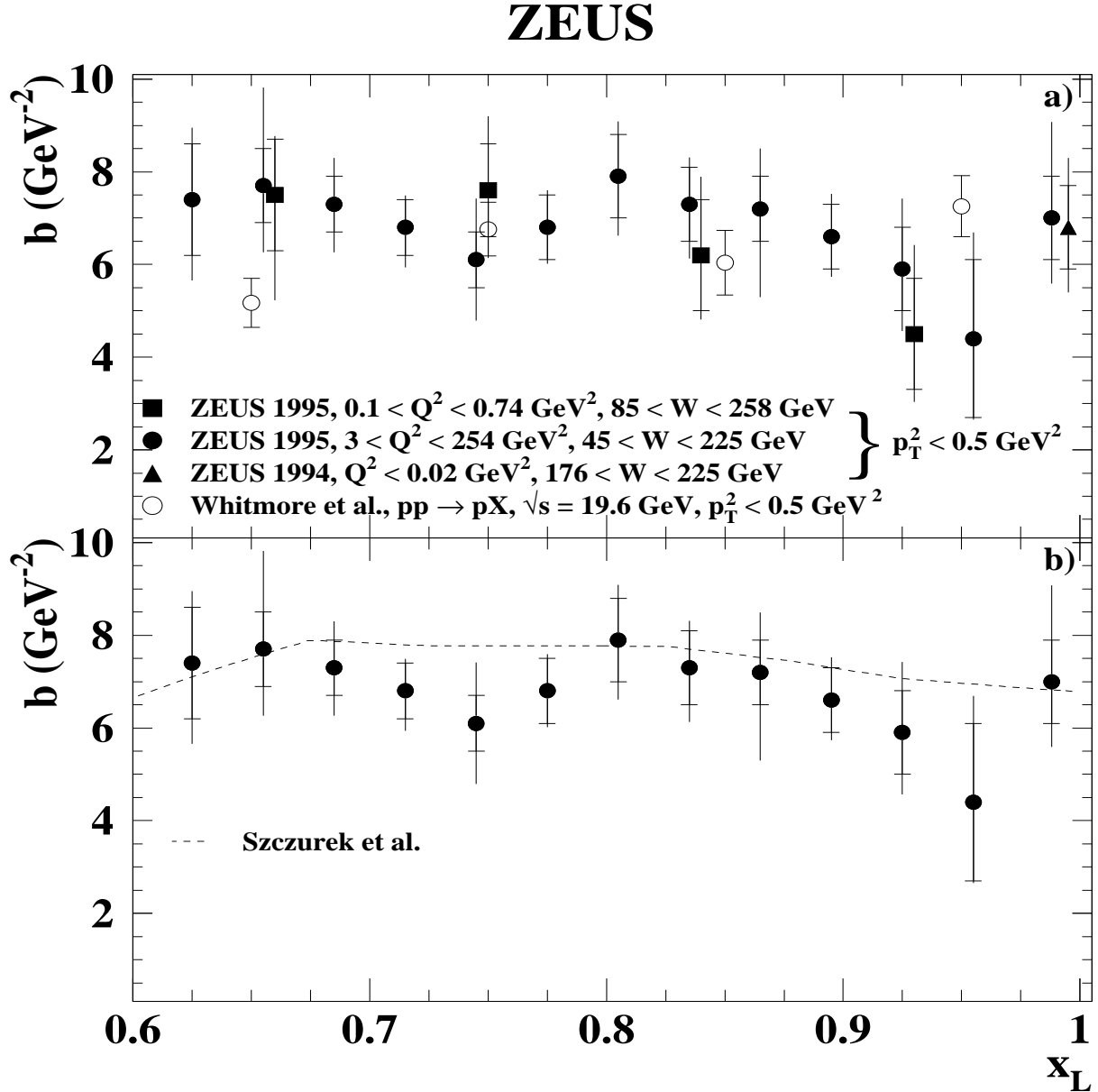


Figure 11: a) The slopes, b , of the p_T^2 distributions for leading protons as a function of x_L for the BPC and DIS data samples. For clarity of presentation, the BPC points are plotted slightly shifted in x_L . The inner bars indicate the statistical uncertainties and the outer are the statistical and systematic uncertainties summed in quadrature. The photoproduction result at $x_L \simeq 1$ is also shown, as are the data from the reaction $\text{pp} \rightarrow \text{pX}$ at $\sqrt{s} = 19.6 \text{ GeV}$. b) The slopes, b , of the p_T^2 distributions for leading protons as a function of x_L for the DIS data sample, compared with the prediction of Szczurek et al. (dashed line).

ZEUS

- **ZEUS 1995, $0.1 < Q^2 < 0.74 \text{ GeV}^2$**
 $85 < W < 258 \text{ GeV}$
 $p_T^2 < 0.5 \text{ GeV}^2$

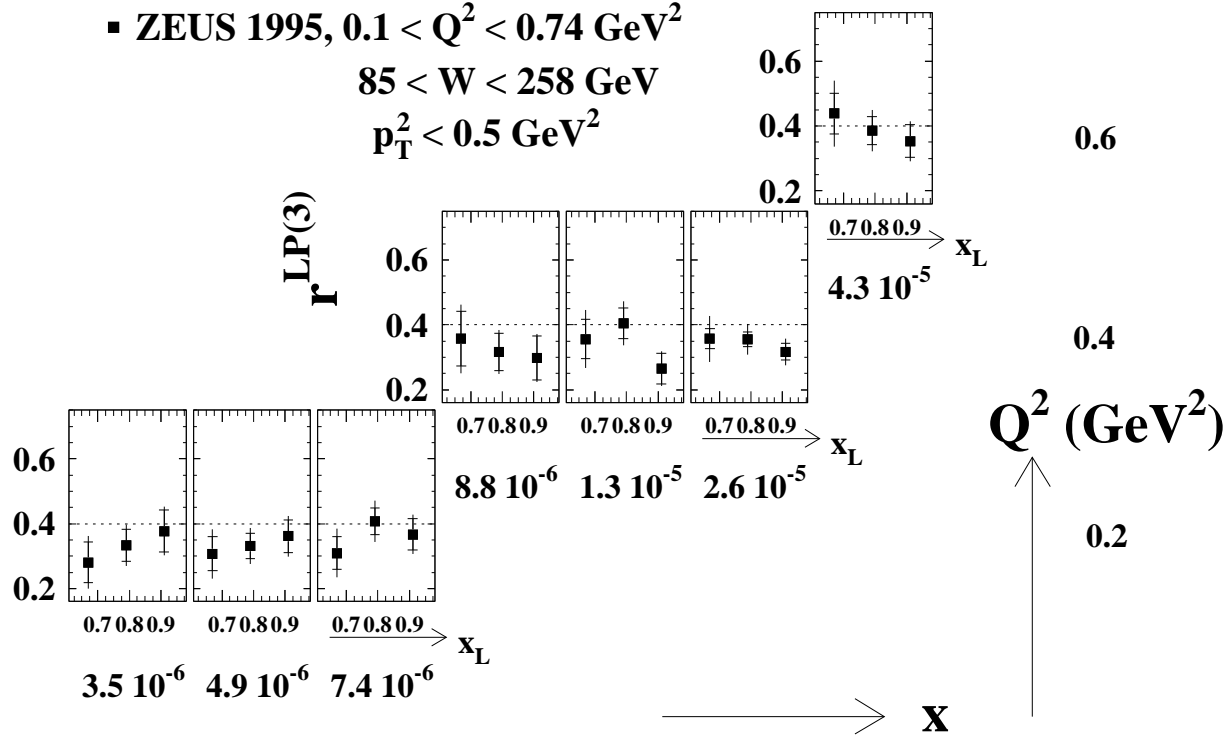


Figure 12: The ratio $r^{\text{LP}(3)} = \bar{F}_2^{\text{LP}(3)}/F_2$ as a function of x_L in bins of x and Q^2 (BPC sample), for protons with $p_T^2 < 0.5 \text{ GeV}^2$. The inner bars show the statistical uncertainties and the outer bars the statistical and systematic uncertainties added in quadrature. The dashed line $r^{\text{LP}(3)} = 0.4$ is overlaid to guide the eye.

ZEUS

- ZEUS 1995, $3 < Q^2 < 254 \text{ GeV}^2$
 $45 < W < 225 \text{ GeV}$
 $p_T^2 < 0.5 \text{ GeV}^2$

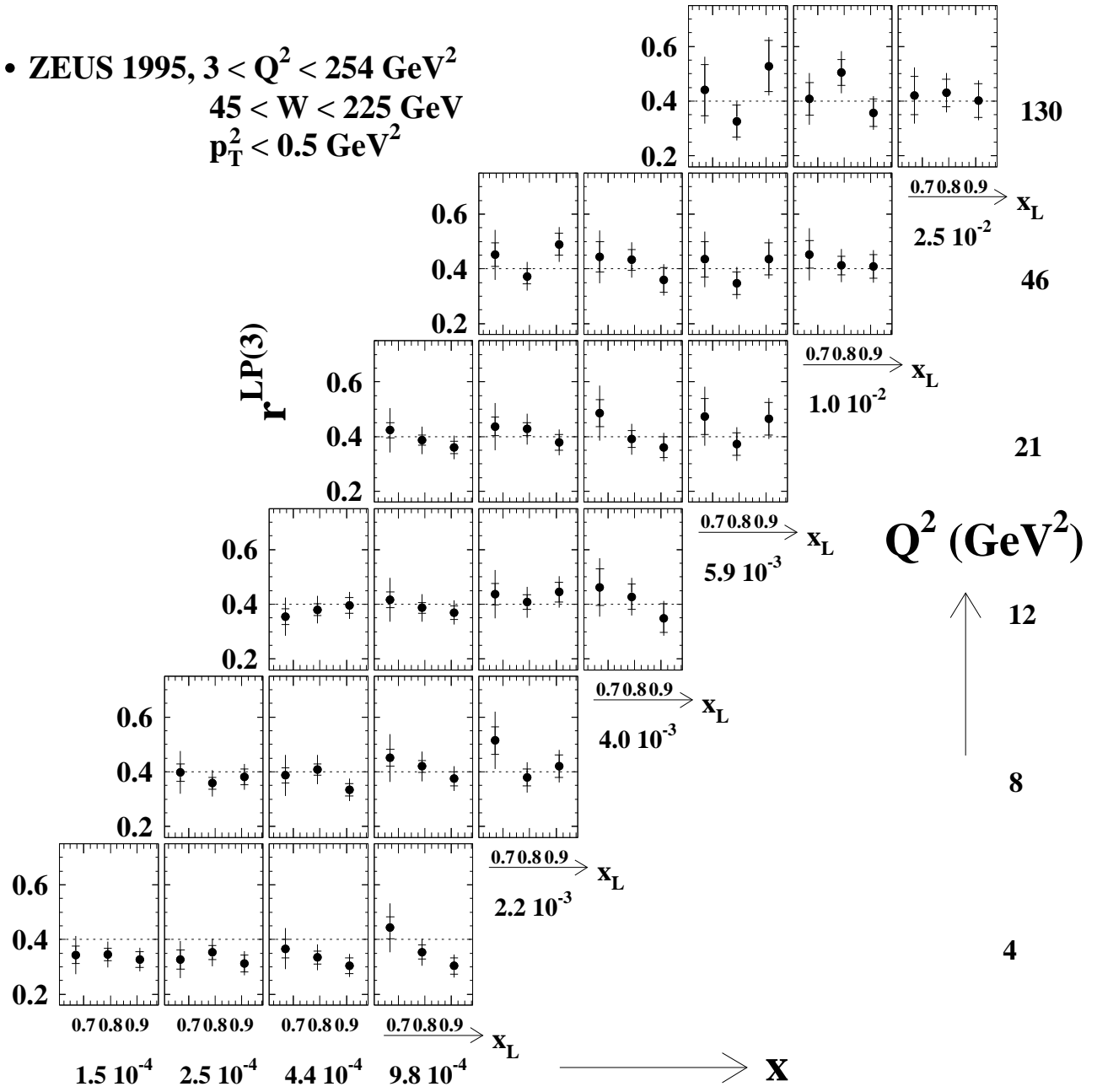


Figure 13: The ratio $r^{LP(3)} = \bar{F}_2^{LP(3)}/F_2$ as a function of x_L in bins of x and Q^2 (DIS sample), for protons with $p_T^2 < 0.5 \text{ GeV}^2$. The inner bars show the statistical uncertainties and the outer bars the statistical and systematic uncertainties added in quadrature. The dashed line $r^{LP(3)} = 0.4$ is overlaid to guide the eye.

ZEUS

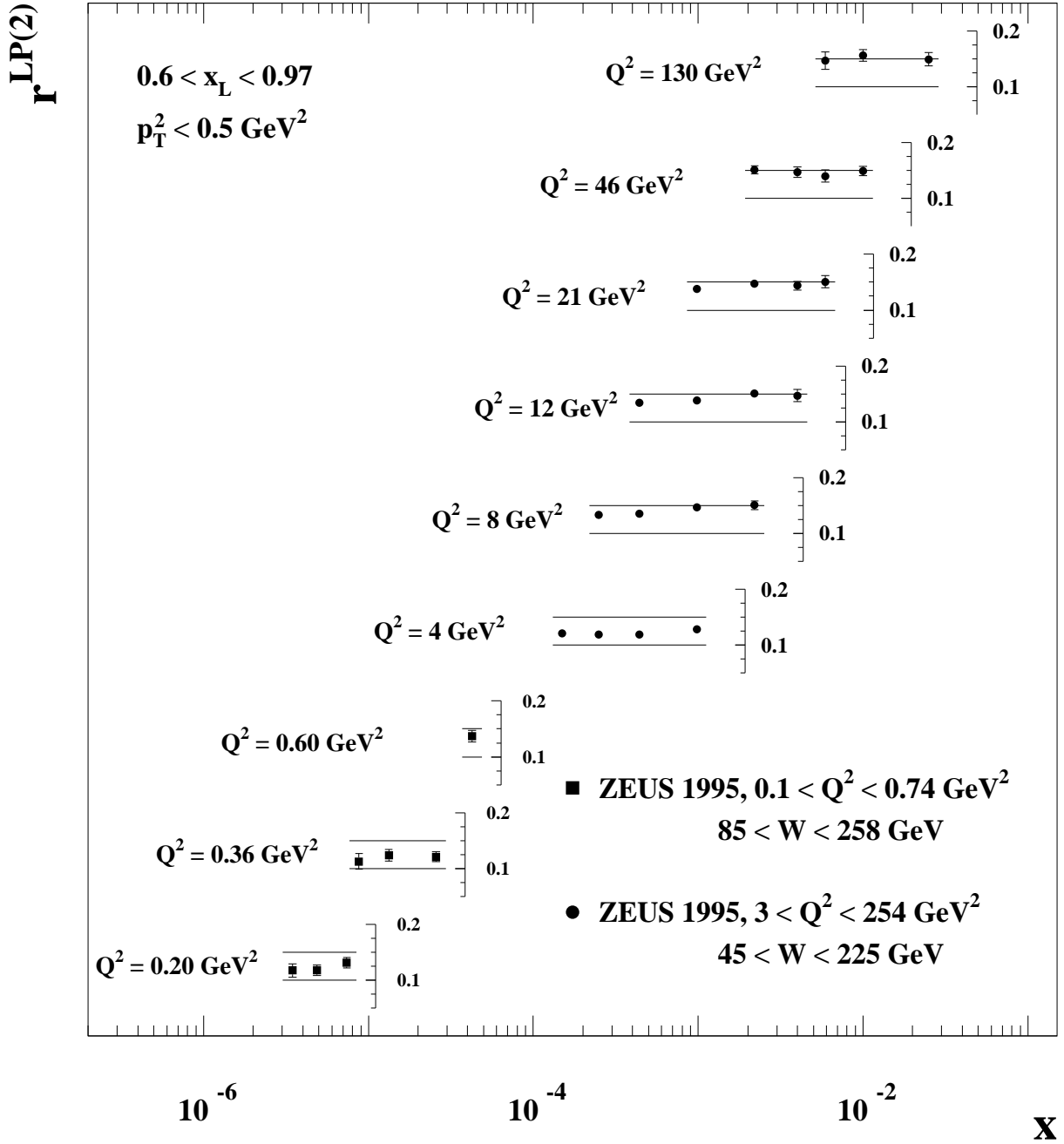


Figure 14: The ratio $r^{\text{LP}(2)} = \bar{F}_2^{\text{LP}(2)}/F_2$ as a function of x for fixed Q^2 values, for protons with $0.6 < x_L < 0.97$ and $p_T^2 < 0.5 \text{ GeV}^2$. The error bars show the statistical uncertainties. A fully correlated systematic uncertainty of $\pm 13\%$ is not shown. The horizontal lines $r^{\text{LP}(2)} = 0.10$ and $r^{\text{LP}(2)} = 0.15$ are overlaid to guide the eye.

ZEUS

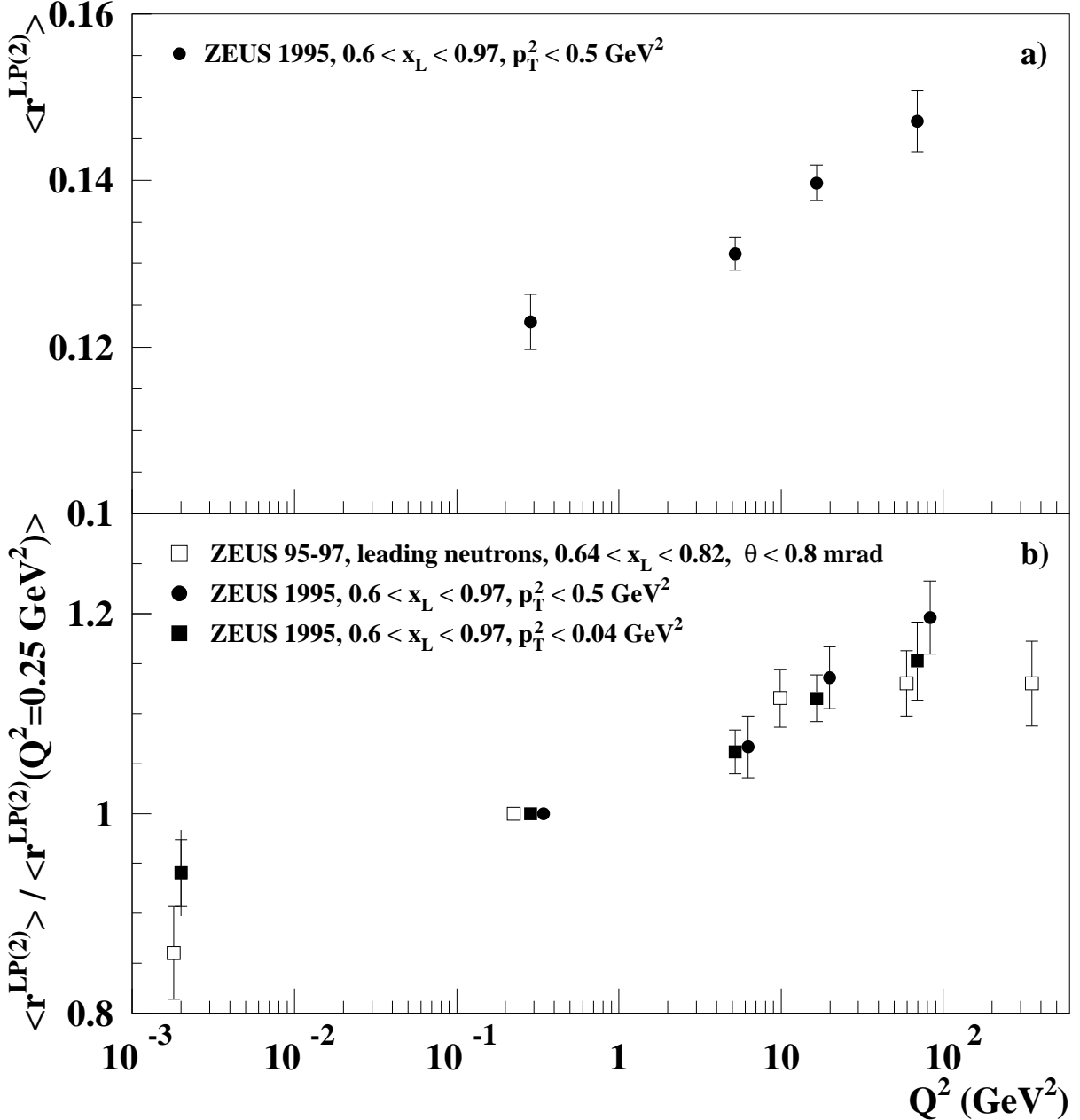


Figure 15: The average ratio $\langle r^{\text{LP}(2)} \rangle = \bar{F}_2^{\text{LP}(2)} / F_2$ as a function of Q^2 . The error bars show the statistical uncertainties. A fully correlated systematic uncertainty of 13% is not shown. a) $\langle r^{\text{LP}(2)} \rangle$ for the range $0.6 < x_L < 0.97$ and $p_T^2 < 0.5 \text{ GeV}^2$. b) $\langle r^{\text{LP}(2)} \rangle$ as a function of Q^2 for two different p_T^2 ranges normalised to the value at $Q^2 = 0.25 \text{ GeV}^2$. The error bars show the statistical uncertainties; systematic errors mostly cancel in the ratio. The ZEUS data for leading neutron production, also normalised to the value at $Q^2 = 0.25 \text{ GeV}^2$, are also shown. The points for $p_T^2 < 0.5 \text{ GeV}^2$ are slightly shifted for clarity of presentation.

ZEUS

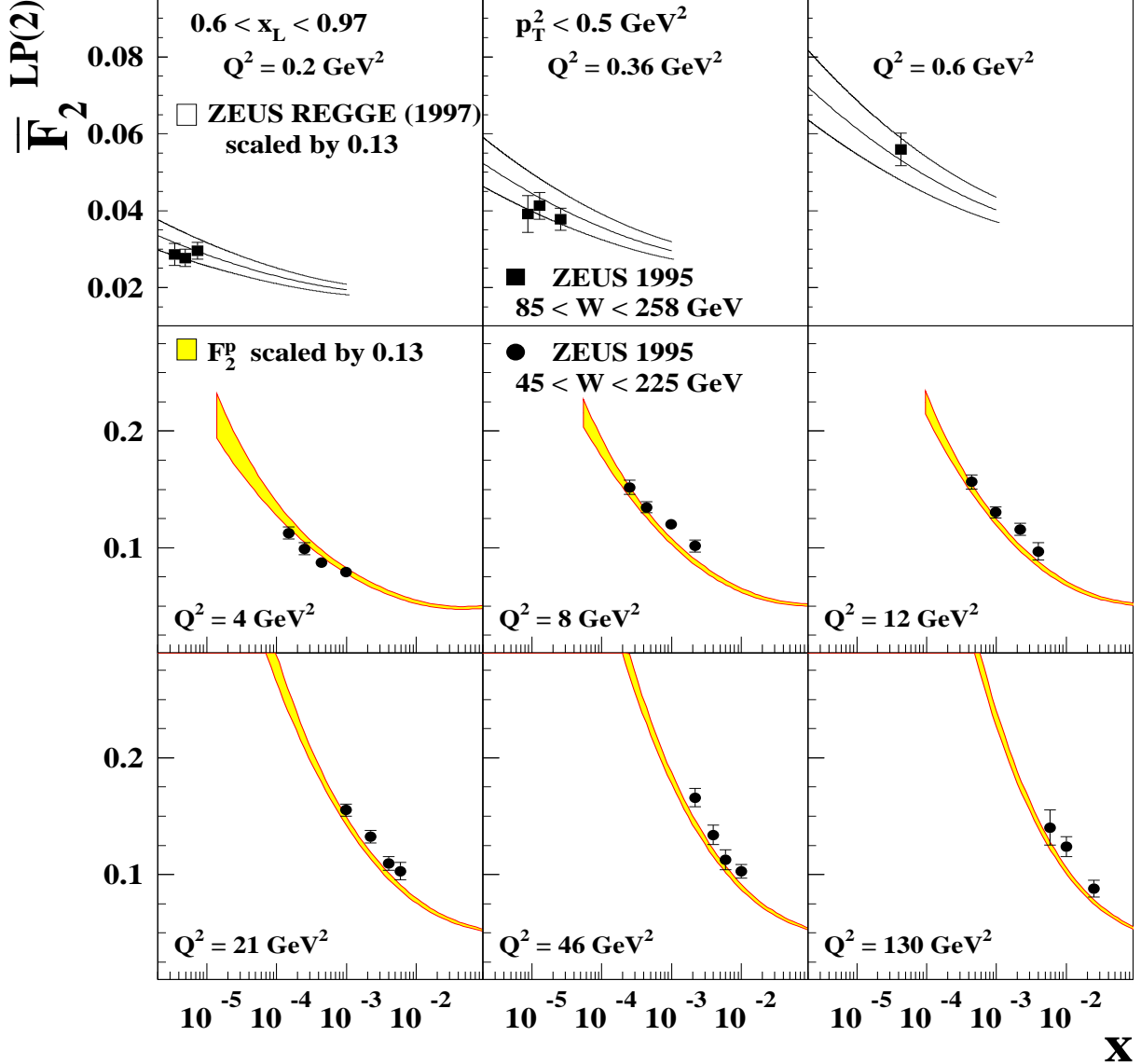


Figure 16: The structure-function $\bar{F}_2^{\text{LP}(2)}$ as a function of x for $0.6 < x_L < 0.97$ and $p_T^2 < 0.5 \text{ GeV}^2$. The bands show the one-standard-deviation limits of the F_2 parametrisations used, scaled by the average value of $r^{\text{LP}(2)}$ ($\langle r^{\text{LP}(2)} \rangle \simeq 0.13$). The error bars show the statistical uncertainties. A fully correlated systematic uncertainty of $\pm 13\%$ is not shown.

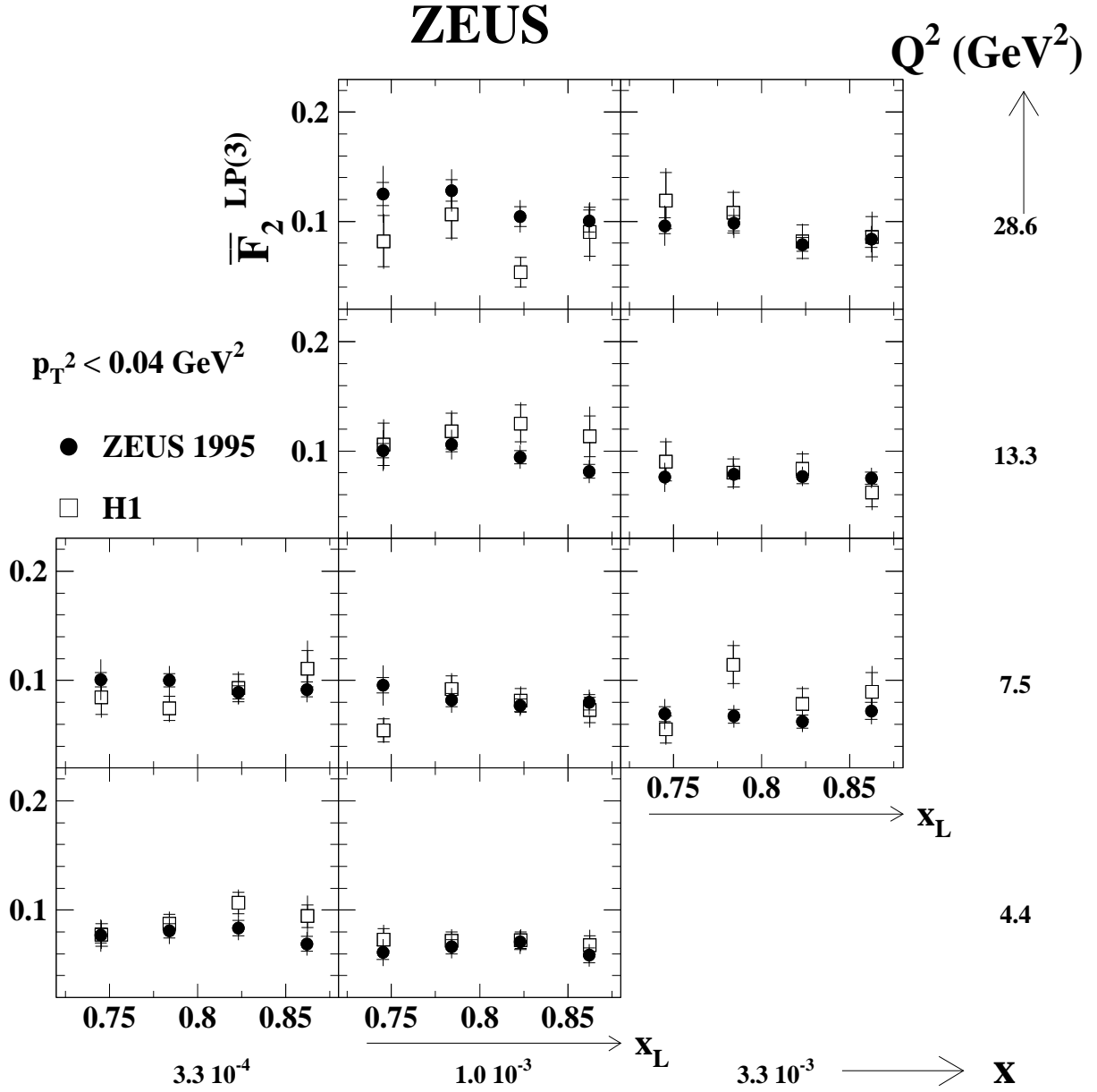


Figure 17: The structure function $F_2^{\text{LP}(3)}$ as a function of x_L in bins of x and Q^2 (DIS sample), for protons in a restricted p_T^2 range, $p_T^2 < 0.04 \text{ GeV}^2$. The inner bars show the statistical uncertainties and the outer bars are the statistical and systematic uncertainties added in quadrature. The H1 results [5] are also shown.

ZEUS

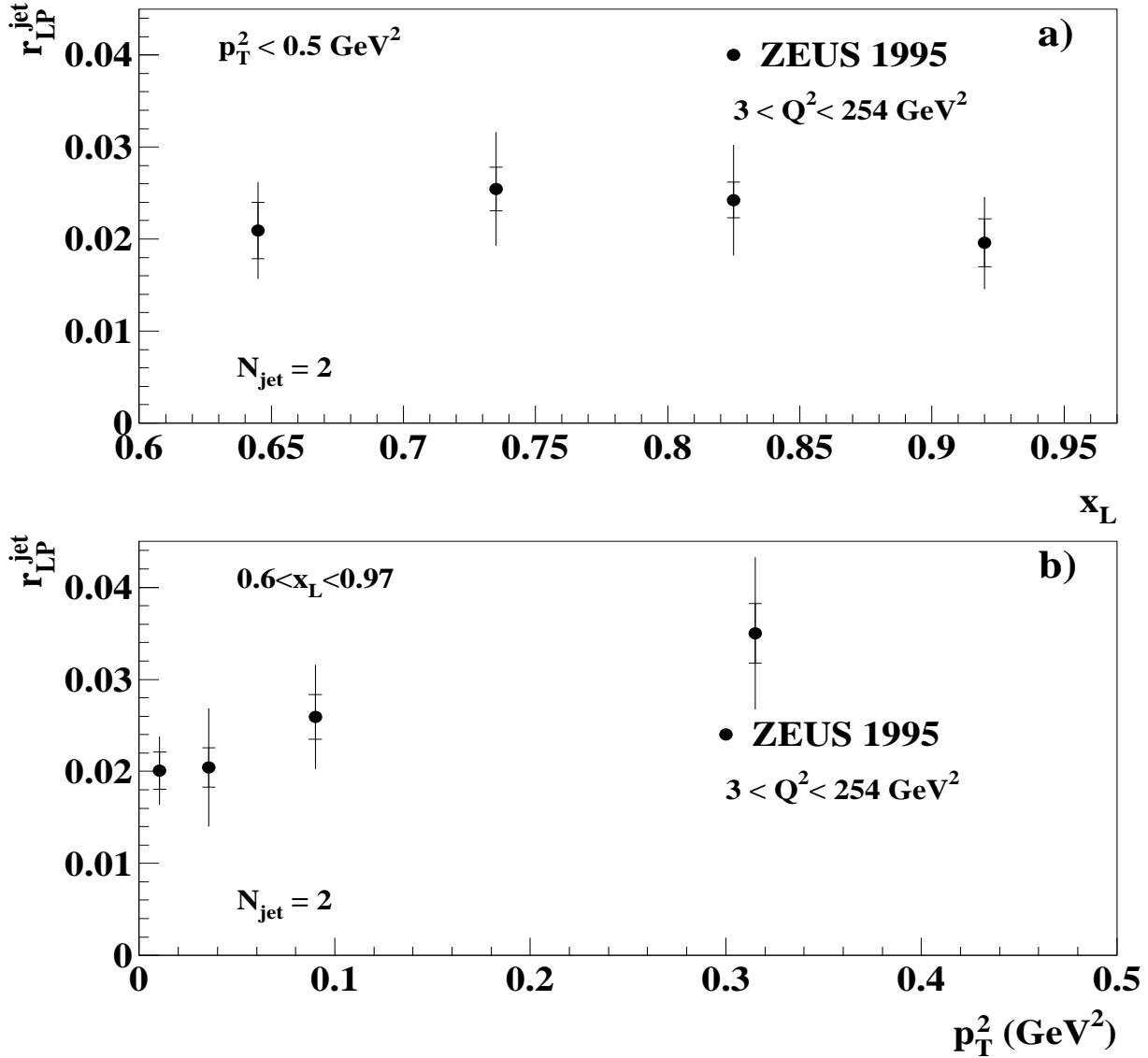


Figure 18: Fraction of leading-proton DIS events with exactly two jets with $E_T > 4 \text{ GeV}$, r_{LP}^{jet} , as a function of a) x_L for $p_T^2 < 0.5 \text{ GeV}^2$ and b) p_T^2 for $0.6 < x_L < 0.97$. The inner bars show the statistical uncertainties and the outer bars show the statistical and systematic uncertainties added in quadrature. The systematic uncertainties are highly correlated.

ZEUS

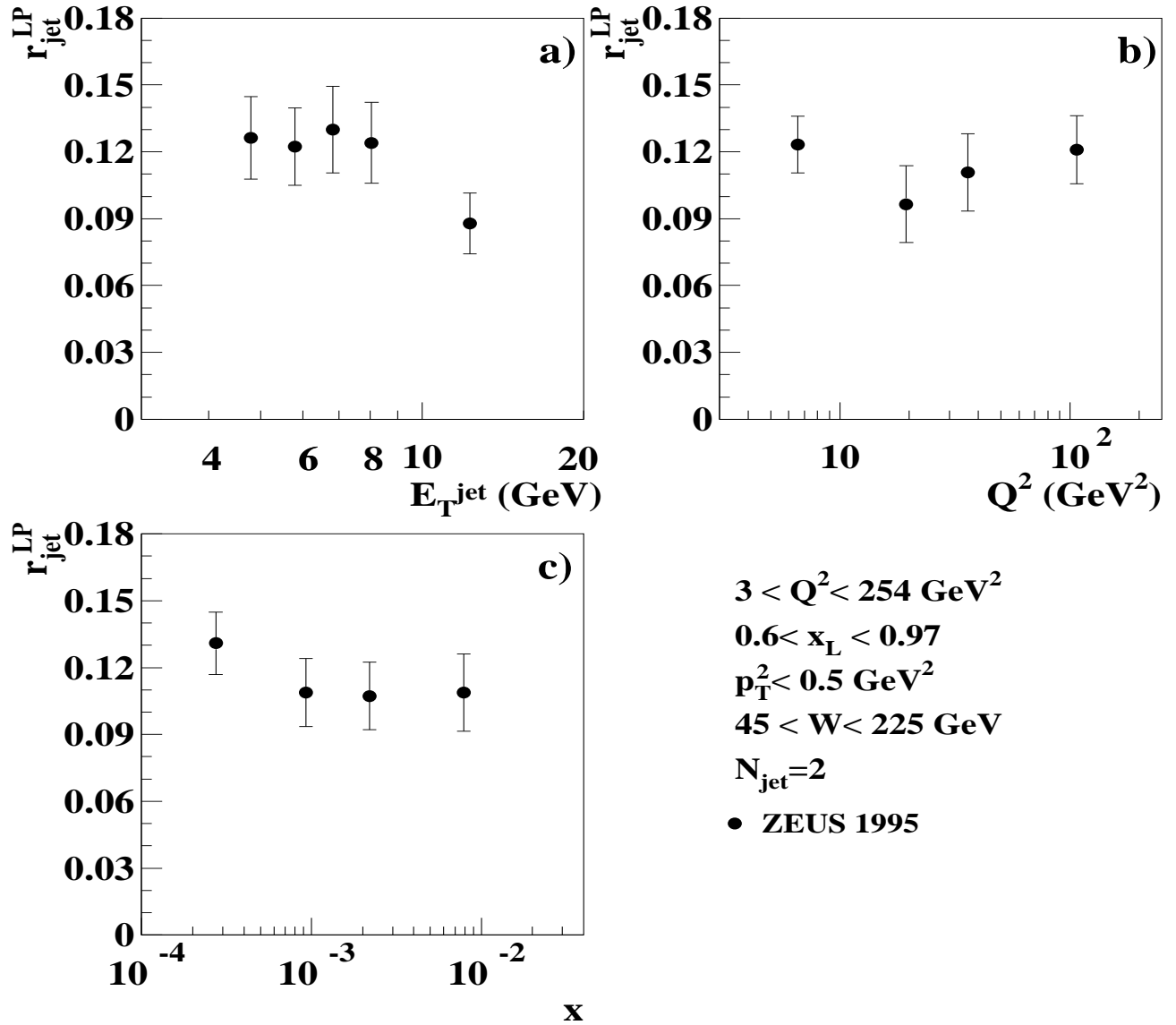


Figure 19: Ratio of the yield of DIS events with exactly two jets with $E_T > 4 \text{ GeV}$ and an LPS proton to the yield of DIS events with exactly two jets, also with $E_T > 4 \text{ GeV}$, $r_{\text{jet}}^{\text{LP}}$, as a function of a) E_T of the higher-energy jet, b) Q^2 and c) x . The error bars show the statistical uncertainties. A fully correlated systematic uncertainty of $\pm 13\%$ is not shown.